ADVANCED FUNCTIONAL MATERIALS
www.afm-journal.de

Secondary-Phase-Induced Charge–Discharge Performance Enhancement of Co-Free High Entropy Spinel Oxide Electrodes for Li-Ion Batteries

Thi Xuyen Nguyen, Jagabandhu Patra, Chia-Chien Tsai, Wen-Ye Xuan, Hsin-Yi Tiffany Chen, Matthew S. Dyer, Oliver Clemens, Ju Li, Subhasish Basu Majumder, Jeng-Kuei Chang, and Jyh-Ming Ting**

High entropy oxide (HEO) has emerged as a new class of anode material for Li-ion batteries (LIBs) by offering infinite possibilities to tailor the charge–discharge properties. While the advantages of single-phase HEO anodes are realized, the effects of a secondary phase are overlooked. In this study, two kinds of Co-free HEOs are prepared, containing Cr, Mn, Fe, Ni, and Zn, for use as LIB anodes. One is a plain cubic-structure high entropy spinel oxide HESO (C) prepared using a solvothermal method. The other HESO (C+T) contains an extra secondary phase of tetragonal spinel oxide and is prepared using a hydrothermal method. It is demonstrated that the secondary tetragonal spinel phase introduces phase boundaries and defects/oxygen vacancies within HESO (C+T), which improve the redox kinetics and reversibility during electrode lithiation/delithiation. Density functional theory calculation is performed to assess the phase stability of cubic spinel, tetragonal spinel, and rock-salt structures, and validate the cycling stability of the electrodes upon charging–discharging. The secondary-phase-induced rate capability and cyclability enhancement of HEO electrodes are for the first time demonstrated. A HESO (C+T)||$LiNi_{0.8}Co_{0.1}Mn_{0.1}O_2$ full cell is assembled and evaluated, showing a promising gravimetric energy density of ≈610 Wh kg^{-1} based on electrode-active materials.

1. Introduction

The skyrocketing energy demand, continuous exhaustion of fossil fuels, and their hazardous by-products have led to the search for green energy resources.[1] Developing environmentally friendly and sustainable alternative energy technologies is thus called for. Among these technologies, lithium-ion batteries (LIBs) play a pivotal role in portable electronics, rechargeable devices, and electric/hybrid vehicles.[2] The negative electrode in a LIB is an essential component that is critical in determining the energy and power densities. However, the conventional graphite anode can only provide a capacity of ≈350 mAh g^{-1}, which no longer satisfies the future demands.[3] Due to the thirst for a higher energy density, new anode materials having higher specific capacity and cyclability continue to be of great interest. Transition metal oxide (TMO) is a typical conversion anode material for LIBs. TMO provides

T. X. Nguyen, C.-C. Tsai, J.-M. Ting
Department of Materials Science and Engineering
National Cheng Kung University
1 University Road, Tainan 70101, Taiwan
E-mail: jting@mail.ncku.edu.tw

J. Patra, J.-K. Chang, J.-M. Ting
Hierarchical Green-Energy Materials (Hi-GEM) Research Center
National Cheng Kung University
1 University Road, Tainan 70101, Taiwan
E-mail: jkchang@nycu.edu.tw

J. Patra, J.-K. Chang
Department of Materials Science and Engineering
National Yang Ming Chiao Tung University
1001 University Road, Hsinchu 30010, Taiwan

W.-Y. Xuan, H.-Y. T. Chen
Department of Engineering and Systems Science
National Tsing Hua University
Hsinchu 300044, Taiwan

The ORCID identification number(s) for the author(s) of this article can be found under https://doi.org/10.1002/adfm.202300509.

DOI: 10.1002/adfm.202300509

W.-Y. Xuan, M. S. Dyer
School of Chemistry
University of Liverpool
Crown St, Liverpool L69 7ZD, UK

W.-Y. Xuan, M. S. Dyer
Materials Innovation Factory
University of Liverpool
51 Oxford St, Liverpool L7 3NY, UK

O. Clemens
Institut für Materialwissenschaft, Chemische Materialsynthese
Universität Stuttgart
Heisenbergstraße 3 70569, Stuttgart, Germany

J. Li
Department of Nuclear Science and Engineering and Department of Materials Science and Engineering
Massachusetts Institute of Technology
77 Massachusetts Avenue, Cambridge, MA 02139, USA

S. B. Majumder
Materials Science Centre
Indian Institute of Technology
Kharagpur, West Bengal 721302, India

large theoretical capacity due to the multi-electron transition during the redox process.[4,5] However, the drawbacks of low conductivity and large volume variation during the lithiation/delithiation process result in unsatisfactory rate performance and poor cycling stability.[6] Transition metal spinel oxide with two Wyckoff sites of octahedral and tetrahedral lattices offers a unique 3D Li^+ transport pathway. The multiple valance states of metal cations in the spinel structure provide charge compensation for reversible Li^+ storage during charging/discharging.[7] The crystal structure of spinel oxide AB_2O_4 is normally composed of divalent metal cations occupying the tetragonal (A) site and trivalent metal cations occupying the octahedral (B) site to form a cubic close-packed configuration. The interchange of the cations in the two crystallographic sites causes the formation of a tetragonal symmetry.[8–10] Both cubic and tetragonal spinel oxides have been investigated as anode materials in LIBs. For example, Sanad et al. compared the electrochemical performance of tetragonal $CoMn_2O_4$ and cubic $MnCo_2O_4$ spinel oxides.[11] The tetragonal $CoMn_2O_4$ showed lower charge transfer resistance and Li^+ diffusion impedance, and better cyclability than that of cubic $MnCo_2O_4$.

Recently, a new class of high entropy oxide (HEO) has appeared as a potential candidate for LIB anodes.[12–20] The HEO composes of five or more metallic constituents with relatively high concentrations (5–35 at.%). Sarkar et al. reported rock-salt (CoCuMgNiZn)O as a LIB anode. The electrode exhibited stable cyclability for 500 cycles without capacity fading.[21] An anode made out of $Mg_{0.2}Co_{0.2}Ni_{0.2}Cu_{0.2}Zn_{0.2}O$ nanoparticles synthesized via a solid-state reaction delivered outstanding cyclability and a reversible capacity of 920 mAh g^{-1} at 100 mA g^{-1} after 300 cycles.[22] Novel high entropy spinel oxide nanoparticles containing cations of Cr, Mn, Fe, Co, and Ni were synthesized using a surfactant-assisted hydrothermal method.[23] This high entropy spinel oxide, without inactive Mg, not only showed an extraordinary charge–discharge capacity of 1235 mAh g^{-1} but also exhibited a high capacity retention of 90% after 200 cycles. Although HEO anodes exhibit excellent performances, most of them contain cobalt (Co). Co-based electrode materials attract much attention as LIB electrodes due to their high conductivity, high redox activity, and great structural stability.[24,25] However, the toxicity, scarcity, aggressively increased price of Co, and geopolitical constraints limit the use of Co. In the long run, replacing Co becomes apparent.[26,27] Chen et al. synthesized a $(Mg_{0.2}Ti_{0.2}Zn_{0.2}Cu_{0.2}Fe_{0.2})_3O_4$ spinel oxide anode, showing a reversible capacity of 504 mAh g^{-1} at 100 mA g^{-1} after 300 cycles.[28] A Co-free high entropy spinel oxide anode of $(CrNiMnFeCu)_3O_4$ showed a great high-rate capacity of 480 mAh g^{-1} at 2000 mA g^{-1}, and excellent cyclic stability was demonstrated as there was no capacity decay after 400 cycles.[26]

With growing attention being paid to HEO anodes, it appears that the positive effect of single-phase HEOs has been realized. Also, some reports showed that a secondary phase gave negative results or simply ignored the presence of the impurity phase.[18,26,29,30] Herein, the effects of a secondary phase on the LIB performance are studied. We use two different wet-chemistry methods to prepare Co-free high entropy spinel oxides (HESOs) consisting of Cr, Mn, Fe, Ni, and Zn. The HESO synthesized via a solvothermal method shows a single-phase cubic spinel structure; while the hydrothermal-synthesized HESO has a major phase of cubic spinel accompanied by a minor tetragonal spinel. We demonstrate that the minor tetragonal phase sustains after cycling and largely reduces the morphology deterioration of the HESO anode due to the improved reversibility, which contributes to the enhanced cyclability. Moreover, this dual-phase HESO shows a higher specific capacity and better rate capability than those of the single-phase HESO. This is the first time that the effects of a secondary phase in HEO on the electrochemical properties have been investigated. It therefore provides a useful guideline for designing new high-performance HEO electrode materials in the future.

2. Results and Discussion

HESOs consisting of identical constituent metals, namely Cr, Mn, Fe, Ni, and Zn, were prepared using solvothermal and hydrothermal methods. The crystal structure of the HESO samples annealed at 900 °C was examined using X-ray diffractometer (XRD), as shown in **Figure 1**a,b. Rietveld refinement of the XRD data shows that the HESO (C) is a single-phase cubic spinel oxide (space group Fd-3m) having a lattice parameter of 8.34 Å. For the HESO (C+T), a secondary phase of tetragonal spinel oxide (space group I41/amd) with a fraction of 12% was found. The details of the Rietveld refinement are given in Table S1–S3 (Supporting Information). XRD analysis was also performed to study the effects of annealing temperature on the crystal structures. For the HESO (C), the as-solvothermal-synthesized state is metal hydroxide (JCPDS#22-0346) with low crystallinity (Figure S1, Supporting Information). After annealing at 300 °C, the hydroxide decomposes and turns into a single-phase spinel oxide (JCPDS#22-1084). With increasing annealing temperature up to 1000 °C, the crystal phase sustains and the crystallinity sharply increases. Meanwhile, after the hydrothermal process, the HESO (C+T) exhibits a hexagonal metal carbonate phase (JCPDS#29-0696). In contrast to the hydroxide, the carbonate remains after annealing at 300 °C. At 600 °C, the metal carbonate is converted to metal oxide with two phases of cubic and tetragonal spinel oxides. The HESO (C+T) remains a two-phase crystal structure having increasing crystallinity with the annealing temperature up to 1000 °C. Thermogravimetric analysis (Figure S2, Supporting Information) was performed to examine the thermal stability of the as-synthesized HESO (C) and HESO (C+T). It is seen that the thermal stabilities of the two as-synthesized samples are not the same. Similar weight losses (≈10%) before 200 °C for both samples are due to the removal of hydration water.[31] After that, the HESO (C) has a significant weight loss between 200 °C and 450 °C, which is ascribed to the decomposition of

S. B. Majumder
Department of Industrial and Manufacturing Systems Engineering
Kansas State University
Manhattan, KS 66506, USA
J.-K. Chang
Department of Chemical Engineering
Chung Yuan Christian University
200 Chung Pei Road, Taoyuan 32023, Taiwan

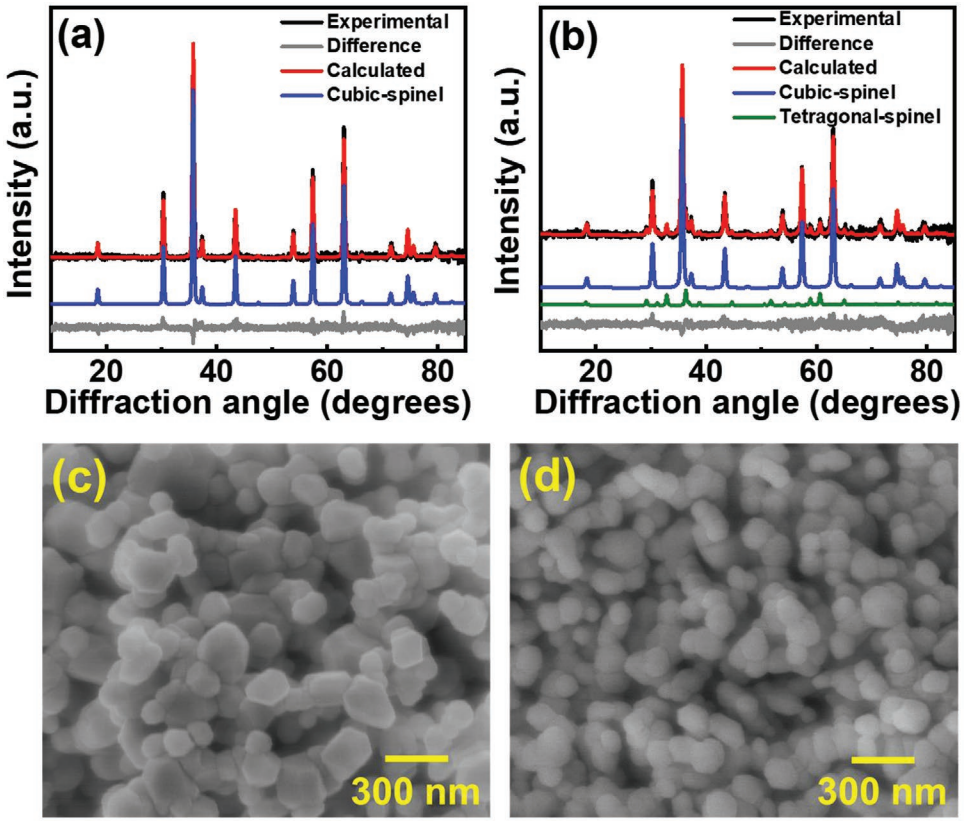

Figure 1. XRD patterns with Rietveld fitting of a) HESO (C) and b) HESO (C+T). SEM images of c) HESO (C) and d) HESO (C+T).

metal hydroxide to become spinel oxide. At the same temperature range, the weight loss of HESO (C+T) is less than that of HESO (C). A higher temperature is required to decompose the metal carbonate, as compared to the metal hydroxide. Scanning electron microscopy (SEM) images (Figure 1c,d) show that both HESO (C) and HESO (C+T) are nanoparticles. The particle size of HESO (C) (≈134 nm) is slightly bigger than that of HESO (C+T) (≈121 nm), as shown in Figure S3 (Supporting Information). The morphology of HESO (C) and HESO (C+T) annealed at different temperatures (800, 900, and 1000 °C) is shown in Figure S4 (Supporting Information). The particle size becomes bigger with increasing annealing temperature and significant agglomeration occurs at 1000 °C. To avoid the agglomeration that can deteriorate the electrode performance, annealing temperature of 900 °C was chosen for the electrode material preparation. Transmission electron microscopy (TEM) analysis of HESO (C) is shown in **Figure 2**. The TEM image (Figure 2a) further confirms the nanoparticle morphology of the HESO (C). High-resolution TEM (HRTEM) images (Figure 2b,c) show lattice spacings of 0.49 and 0.29 nm, corresponding to the (111) and (220) planes of the cubic spinel oxide, respectively. The selected area electron diffraction (SAED) pattern (Figure 2d) is well-indexed to single-phase spinel structure. Scanning TEM (STEM) energy-dispersive X-ray spectroscopy (EDS) elemental mapping of the HESO (C), as shown in Figure 2e, indicates the distribution of Cr, Mn, Fe, Ni, Zn, and O elements. TEM image of HESO (C+T) nanoparticles is displayed in **Figure 3**a. As shown in Figure 3b, two phases are seen, showing a clear view of a phase boundary. The lattice fringes corresponding to the cubic spinel phase are shown in Figure 3c. Tetragonal spinel oxide with a space group of I41/amd is also identified (Figure 3d). Figure 3e,f are the corresponding nanobeam diffraction patterns of the imaged area shown in Figure 3c,d, respectively. The diffraction pattern in Figure 3e indicates a cubic spinel structure, while that in Figure 3f is indexed as a tetragonal spinel phase. The TEM diffraction pattern in Figure 3g shows the co-existence of cubic and tetragonal spinel phases. STEM-EDS analysis shows the elemental distribution in HESO (C+T) (Figure 3h). To examine the composition difference of the two phases in HESO (C+T), high spatial-resolution EDS measurements were conducted at different positions in the tetragonal and cubic phases. The obtained data are shown in Figure S5 and Table S4 (Supporting Information). The EDS beam size is ≈3 nm, which is smaller than the domain size of both phases. In the tetragonal phase, the elemental concentrations are nearly equimolar. In contrast, in the cubic phase, a higher concentration of Cr and a clearly lower concentration of Mn were detected. Then, the EDS elemental concentrations of the two phases were taken to calculate the entropy values. The entropy values of the cubic and tetragonal phases in HESO (C+T) are 1.56 and 1.60 R, respectively. Both phases are thus qualified as high entropy materials. The chemical compositions of the samples were quantitatively determined via inductively coupled plasma-mass spectrometry (ICP-MS). As shown in Table S5 (Supporting Information). The elemental concentrations in HESO (C+T) are close to equimolar; while the

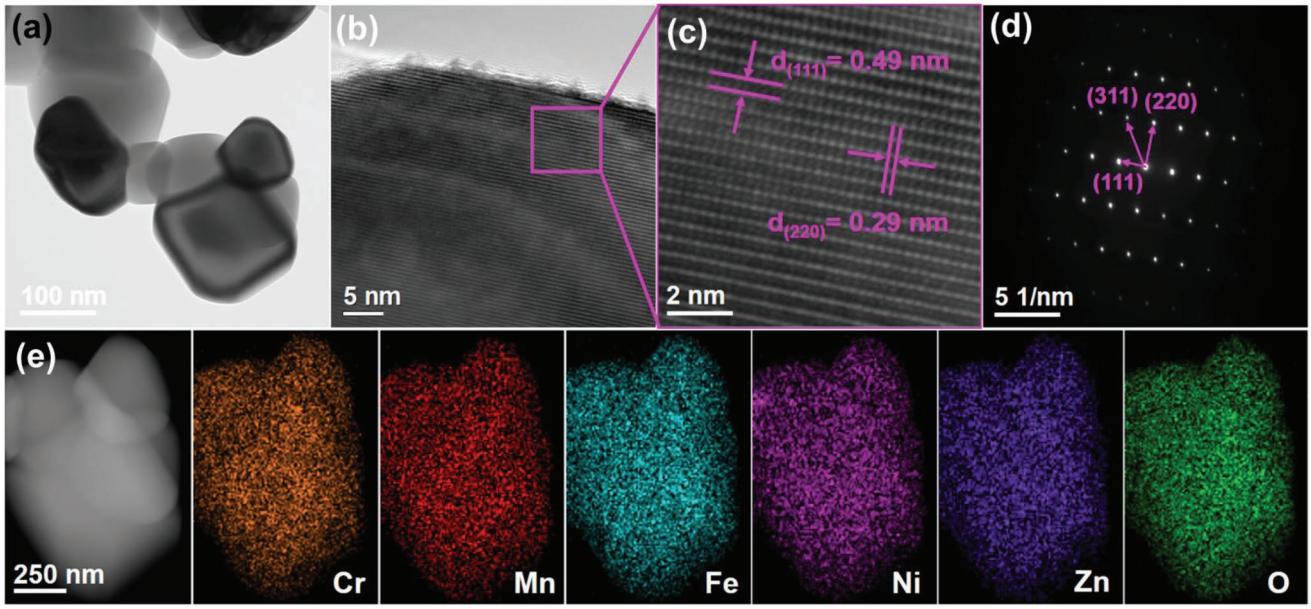

Figure 2. a) TEM image, b,c) HRTEM images, d) SAED pattern, and e) STEM-EDS elemental mapping of HESO (C).

concentration of Mn in HESO (C) is clearly less. The lower content of Mn in HESO (C) is probably due to the higher solubility of $Mn(OH)_2$ (compared to that of the other metal hydroxides) in ethylene glycol.[32]

To have a better understanding of the phase formation and structural stability of HESO (C) and HESO (C+T) based on the consideration of chemical composition, density functional theory (DFT) calculations have been performed. The detailed methodology to determine the high entropy material configurations is provided in the Supporting Information. The quasi-random models after basin hopping calculations of HESO (C) and HSEO (C+T) for cubic spinel, tetragonal spinel, and rock-salt structures are given in **Figure 4**a–f, with the energy per atom values above the convex hull listed below the structures. As shown, for both materials, the cubic spinel is the most stable structure, whereas the rock-salt configuration is the least stable. These results are well supported by the experimental observations. Although thermodynamically unfavorable, a tetragonal spinel phase formed in HSEO (C+T). This could be associated with the kinetic issues that involve complexation and coordination states of the multiple metal ions in the hydrothermal synthesis. The more detailed mechanism study will be needed to address this matter. It is noted that the multi-phase HSEO (C+T) material has a convex hull energy of = 55 meV/atom × 88% + 120 meV/atom × 12% = 62.8 meV/atom which is close to that (62 meV/atom) of the single-phase HSEO (C). Hence, it is justifiable to obtain the two kinds of crystallinity (i.e., C and C+T) by using the different synthesis routes.

To investigate the surface chemistry, X-ray photoelectron spectroscopy (XPS) analysis was carried out, as shown in **Figure 5**. In the Cr 2p spectra, the peaks at 576.0 eV (Cr $2p_{3/2}$) and 578.5 eV (Cr $2p_{3/2}$) are assigned to Cr^{3+} and Cr^{6+}, respectively.[33] The peak centered at 585.5 eV belongs to a Cr $2p_{1/2}$ orbital peak. The Cr^{3+} and Cr^{6+} exist in both samples with Cr^{3+}/Cr^{6+} ratios of 85.1/14.9 and 84.3/15.7 for HESO (C) and HESO (C+T), respectively. The Mn, Fe, and Ni all have divalent and trivalent oxidation states. The Mn 2p spectra show two major spin-orbital peaks of Mn $2p_{3/2}$ and Mn $2p_{1/2}$ at 642.2 and 653.6 eV, respectively.[34] The Mn $2p_{3/2}$ peaks are fitted into Mn^{2+} at 641.2 eV and Mn^{3+} at 642.6 eV.[35,36] The Mn^{2+}/Mn^{3+} ratios are 40.4/59.6 and 62.5/37.5 for the HESO (C) and HESO (C+T), respectively. The peaks located at 637.6 and 645.2 eV are attributed to the Auger peak and satellite peak, respectively.[37] In the XPS Fe 2p spectra, the peaks at 709.8 eV (Fe $2p_{3/2}$) and 711.6 eV (Fe $2p_{3/2}$) are associated with Fe^{2+} and Fe^{3+}, respectively. Two satellite peaks are found at 714.8 and 718.5 eV.[38] The peak at 724.1 corresponds to the Fe $2p_{1/2}$ orbital peak. The Fe^{2+}/Fe^{3+} ratios are 42.4/57.6 in HESO (C) and 46.1/52.9 in HESO (C+T). In the Ni 2p spectra, the Ni $2p_{3/2}$ and Ni $2p_{1/2}$ orbital peaks are located at 854.8 and 872.4 eV, respectively. HESO (C) has a Ni^{2+}/Ni^{3+} ratio of 68.5/31.5 while this ratio in HESO (C+T) is 63.2/36.8. Two satellite peaks are seen at 861.1 and 879.3 eV.[39,40] Only a divalent state was found in the Zn 2p spectra. The average oxidation states of HESO (C) and HESO (C+T) were calculated to be 2.59 and 2.56, respectively. The O 1s spectra consist of three peaks, which are related to lattice oxygen (O_L), oxygen vacancy (O_V), and chemisorbed oxygen (O_C).[41] The concentration of O_V in HESO (C+T) is higher than that in HESO (C) (30.6% versus 25.5%). The introduction of the secondary tetragonal phase was found to decrease the average valence states of the HESO and thus lead to an increased content of O_V. In addition, electron paramagnetic resonance (EPR) analysis was conducted to examine the Ov content in both samples. As shown in the EPR spectra (Figure S6, Supporting Information), the difference in the peak height depicts that the Ov content in HESO (C+T) is higher than that in HESO (C). The high concetration of Ov can increase the electron hole density, that enhances the electronic conductivity. Furthermore, Ov can promote the Li^+ transport, resulting in superior electrochemical performance.[18,42,43]

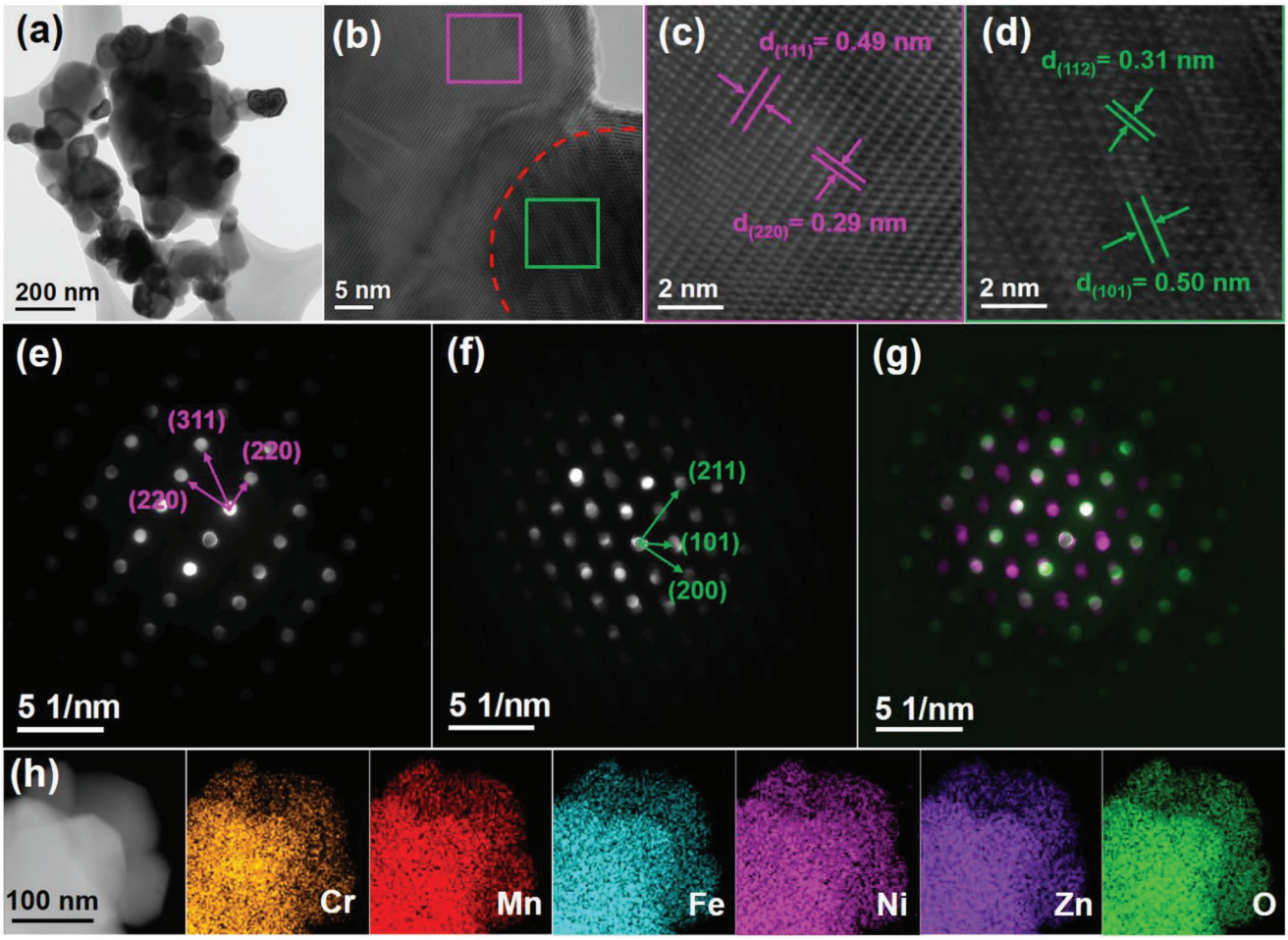

Figure 3. a) TEM image, b–d) HRTEM images, e) nanobeam electron diffraction pattern of (c), f) nanobeam electron diffraction pattern of (d), g) overlapped diffraction patterns of cubic and tetragonal spinel phases, and h) STEM-EDS elemental mapping of HESO (C+T).

The cyclic voltammetry (CV) tests were performed to study the lithium-storage properties of the HESO (C) and HESO (C+T) electrodes. The observed curves with various anodic and cathodic peaks, which are associated with Li^+ uptake/release of the electrodes, are shown in Figure S7 (Supporting Information). In the first cathodic (i.e., lithiation) scan for both cells, multiple peaks were observed, corresponding to electrolyte decomposition (thus solid-electrolyte interphase (SEI) formation), reductive conversion reactions, and Li_2O formation.[7,44] In the subsequent anodic scan, the current before ≈1.2 V is steady, indicating that the electrode delithiation rate was nearly constant. There are several overlapping oxidation peaks in the region between 1.2 and 2.5 V, which are related to the re-conversion and/or oxidation of the reduced species produced during the lithiation process.[29,45] The presence of tetragonal phase in HESO (C+T) did not significantly affect the CV characteristic features. In the second cycle, the lithiation reactions are facilitated to launch at ≈1.5 V. It is noted that from the 2nd cycle onward, the succeeding CV curves mostly overlapped, suggesting good electrochemical reversibility and stability of the HESO electrodes.

To evaluate the Li^+ storage properties of the HESO electrodes, galvanostatic charge–discharge tests were performed. Figure S8 (Supporting Information) shows the initial three lithiation-delithiation curves of HESO (C) and HESO (C+T) tested at 50 mA g^{-1}. As shown, the first lithiation curve is characterized by a voltage plateau below ≈0.5 V, which is consistent with the CV result (see Figure S7, Supporting Information) and is linked to the SEI formation and irreversible trapping of Li^+ ions within the electrode. The first-cycle Coulombic efficiency (CE) of HESO (C) and HESO (C+T) electrodes are 69 and 73%, respectively, which are comparable to those reported in the literature for HEOs. We certainly believe that these values can be further increased by optimizing the binder and electrolyte recipes, and by using an upgraded electrode coating process. As exhibited, the lithiation-delithiation behavior became steady after two cycles, with the CE values of both cells being ≈99%. The differential capacity curves (dQ/dV plots) obtained from the first charge–discharge cycles of HESO (C) and HESO (C+T) electrodes are shown in Figure S9 (Supporting Information). The results show that both electrodes exhibit similar dQ/dV curves and insignificant difference in the redox behavior was observed. In addition, electron energy loss spectroscopy (EELS) was performed to further examine the HESO (C) and HESO (C+T) electrodes. The EELS spectra of both electrodes before and after the first charge–discharge cycle are shown

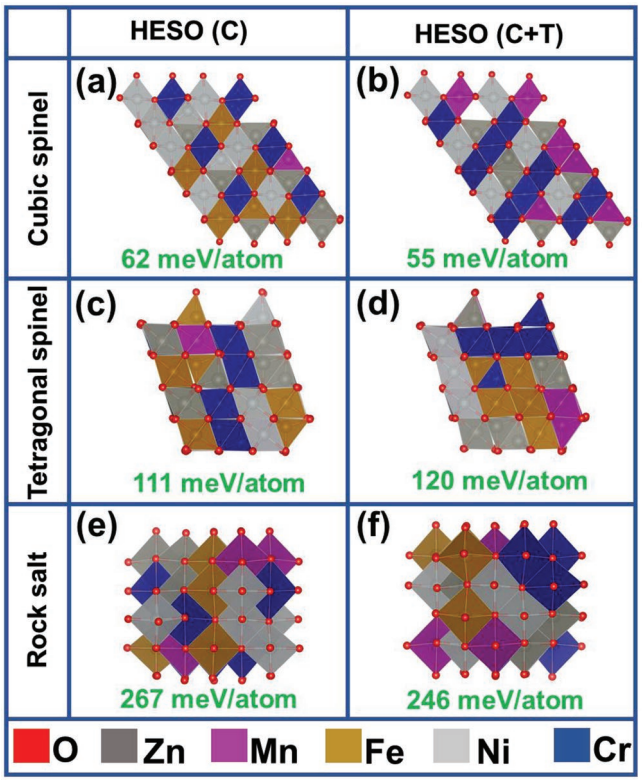

Figure 4. a,b) Most stable configurations of cubic spinel structures, c,d) most stable configurations of tetragonal spinel structures, and e,f) most stable configurations of rock-salt structures with the two chemical compositions. The values listed below the structures are the energy per atom above the convex hull.

in Figure S10 (Supporting Information). The peak position is indicative of the valance state. While high redox reversibility of Cr, Mn, and Fe was found, the Ni seems to be less reversible. According to the results, we conclude that there is no significant difference in the charge storage mechanism between the two electrodes. To examine if both phases in HESO (C+T) participate in the electrochemical reaction, we have performed ex-situ XRD measurement on the electrode after complete lithiation. As shown in Figure S11 (Supporting Information), the results confirm the amorphous nature of the electrode. This indicates the participation of both the cubic and tetragonal phases in the charge storage reactions.

Figure 6a,b show the charge–discharge curves of the HESO (C) and HESO (C+T) electrodes recorded at various current densities. With gradually increasing the rate from 50 to 3000 mA g^{-1}, the specific capacities steadily decreased due to the kinetic limitation of the lithiation/delithiation processes.[46,47] At 50 mA g^{-1}, the reversible capacities of HESO (C) and HESO (C+T) are 830 and 865 mAh g^{-1}, respectively. Both electrodes revealed considerably higher reversible capacities than that (practically ≈350 mAh g^{-1}) of a conventional graphite anode,[48] demonstrating a potential application of this kind of HEO for LIBs. Figure 6c shows the rate capability of the HESO (C) and HESO (C+T) electrodes. At 3000 mA g^{-1}, the measured capacities were 486 and 560 mAh g^{-1}, respectively, corresponding to 59% and 65% retention compared to the capacities obtained at 50 mA g^{-1}. The induced phase boundaries and the higher O_V concentration are mainly responsible for the enhanced electrochemical performance of the HESO (C+T) electrode. In other words, the secondary phase does not alter the charge–discharge mechanism but clearly improves the redox kinetics. Generally, oxide anodes following a conversion-type charge storage mechanism show a substantial capacity deterioration at high current rates owing to their low conductivity and limited kinetics of diffusion-driven redox processes during lithiation/delithiation.[49,50] The excellent rate capability of the HESO (C+T) electrode is among the best performance in the state-of-the-art HEO anodes for LIBs. HESO (C+T) outperforms many most recent reported HEOs in terms of high-rate performance, such as $(Co_{0.2}Cu_{0.2}Mg_{0.2}Ni_{0.2}Zn_{0.2})O$ (≈160 mAh g^{-1}@3000 mA g^{-1}), $(Mg_{0.2}Co_{0.2}Ni_{0.2}Cu_{0.2}Zn_{0.2})O$ (490 mAh g^{-1}@3000 mA g^{-1}), $(Mg_{0.2}Co_{0.2}Ni_{0.2}Cu_{0.2}Zn_{0.2})O$ (408 mAh g^{-1}@2000 mA g^{-1}), $(MgCoNiZn)_{0.65}Li_{0.35}O$ (≈610 mAh g^{-1}@1000 mA g^{-1}), $(Mg_{0.2}Co_{0.2}Ni_{0.2}Cu_{0.2}Zn_{0.2})O$ (≈300 mAh g^{-1}@1800 mA g^{-1}), $(FeNiCrMnMgAl)_3O_4$ (≈400 mAh g^{-1}@2000 mA g^{-1}), $(Mg_{0.2}Co_{0.2}Ni_{0.2}Cu_{0.2}Zn_{0.2})O$@graphene (393 mAh g^{-1}@2000 mA g^{-1}), $(FeCoNiCrMn)_3O_4$ (≈180 mAh g^{-1}@2000 mA g^{-1}), $(FeCoNiCrMnZnLi)_3O_4$ (≈173 mAh g^{-1}@2000 mA g^{-1}), (MgCuNiCoZn)O (240 mAh g^{-1}@2000 mA g^{-1}), $(FeNiCrMnZn)_3O_4$ (≈260 mAh g^{-1}@3000 mA g^{-1}), $(Mg_{0.2}Ti_{0.2}Zn_{0.2}Cu_{0.2}Fe_{0.2})_3O_4$ (≈268 mAh g^{-1}@2000 mA g^{-1}), and $(CrMnFeNiCu)_3O_4$ (≈480 mAh g^{-1}@2000 mA g^{-1}).[7,18,21,22,26,28,29,44,51–55] Table S6 (Supporting Information) shows the performance comparision between HESO (C+T) and previously reported HEO electrodes. Our Co-free HESO (C+T) electrode shows promising specific capacity, rate capability, and cycling stability. The fast lithiation/delithiation reaction of the HESO electrode is highly attractive. This can be attributed to the multiple cation centers and abundant oxygen vacancies that provide high redox activity and plenty of conduction pathways for Li^+ transport.[7,27,52]

The electrochemical impedance spectroscopy (EIS) analysis was carried out to understand the impedance of the HESO (C) and HESO (C+T) electrodes. The spectra shown in Figure 6d were obtained after five CV cycles. The Nyquist plots comprise an intercept at high frequency, a semicircle at intermediate frequency, and a sloping line at low frequency. The equivalent circuit to fit the data is shown in the figure inset. The R_e, R_{ct}, *CPE*, and *W* represents the electrolyte resistance, charge-transfer resistance, interfacial constant phase element, and Warburg impedance corresponding to Li^+ transport in the HESO electrode.[56] The fitting results reveal that the R_{ct} values for the HESO (C) and HESO (C+T) electrodes are 12 and 7 Ω, respectively. The apparent Li^+ diffusion coefficient (D_{Li^+}) can be calculated from the low-frequency sloping line.[57] The HESO (C+T) electrode has a higher D_{Li^+} value of 6.8×10^{-13} cm^2 s^{-1}, compared to 3.5×10^{-13} cm^2 s^{-1} for HESO (C). This is ascribed to the higher O_V concentration of HESO (C+T), which improves both the electronic and ionic conductivities of the electrode.[58,59] The low R_{ct} and high D_{Li^+} values of HESO (C+T) explain its superior charge–discharge rate capability. Additionally, the D_{Li^+} for the electrodes were also evaluated using a galvanostatic intermittent titration technique (GITT). The data are shown in Figure S12 (Supporting Information). As exhibited, the $D_{Li^+(GITT)}$ of HESO (C+T) is evidently higher than that of the HESO (C) electrode, consistent with the EIS results.

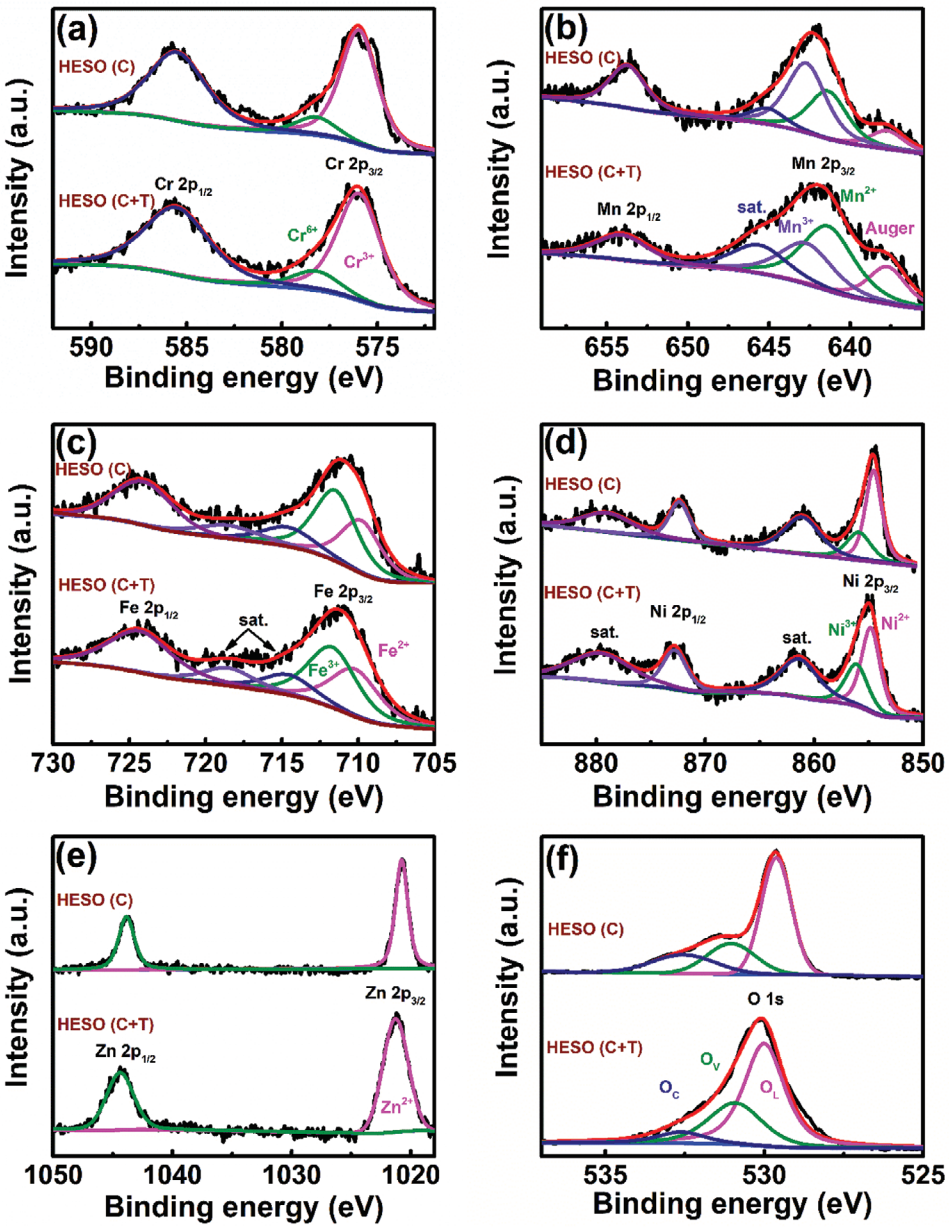

Figure 5. High-resolution XPS spectra of a) Cr 2p, b) Mn 2p, c) Fe 2p, d) Ni 2p, e) Zn 2p, and f) O 1s orbitals of HESO (C) and HESO (C+T) samples.

Figure 7a shows the cycling stability data of both HESO cells after three conditioning cycles measured at a charge–discharge rate of 500 mA g^{-1}. After 200 cycles, the HESO (C) and HESO (C+T) electrodes retained 45% and 90% of the initial capacities, respectively. As shown, the capacity fluctuation during cycling occurred. This feature was also found in other HEO electrodes reported in the literature,[18,21–23,26] which could be ascribed to structural and/or compositional reconfiguration of the multi-element electrode materials. The relatively high O_V content, which promotes phase change reversibility and reduces the lattice stress during lithiation/delithiation,[60,61] can be a reason for the better cycling stability of the HESO (C+T) electrode. Figure 7b shows the EIS spectra of the electrodes after 200 cycles. The R_{ct} values of the HESO (C) and HESO (C+T) electrodes increased to 92 and 47 Ω, respectively. In addition, the D_{Li}^+ values decreased to 1.8×10^{-15} cm^2 s^{-1} and 5.3×10^{-14} cm^2 s^{-1}, respectively. The variation of R_{ct} versus the cycle number for HESO (C) and HESO (C+T) electrodes are shown in Figure S13 (Supporting Information). A clear volume expansion, particle agglomeration, and SEI accumulation are observed for HESO (C) after cycling (Figure 7c), resulting in the electrode performance decay. The superior cyclability of the HESO (C+T) electrode is associated with the less morphology deterioration, as shown in Figure 7d. Of note, this is the first study to reveal that the HEO cyclability can be significantly enhanced by the introduction of a secondary phase of tetragonal spinel oxide. The possible mechanism is discussed as follows.

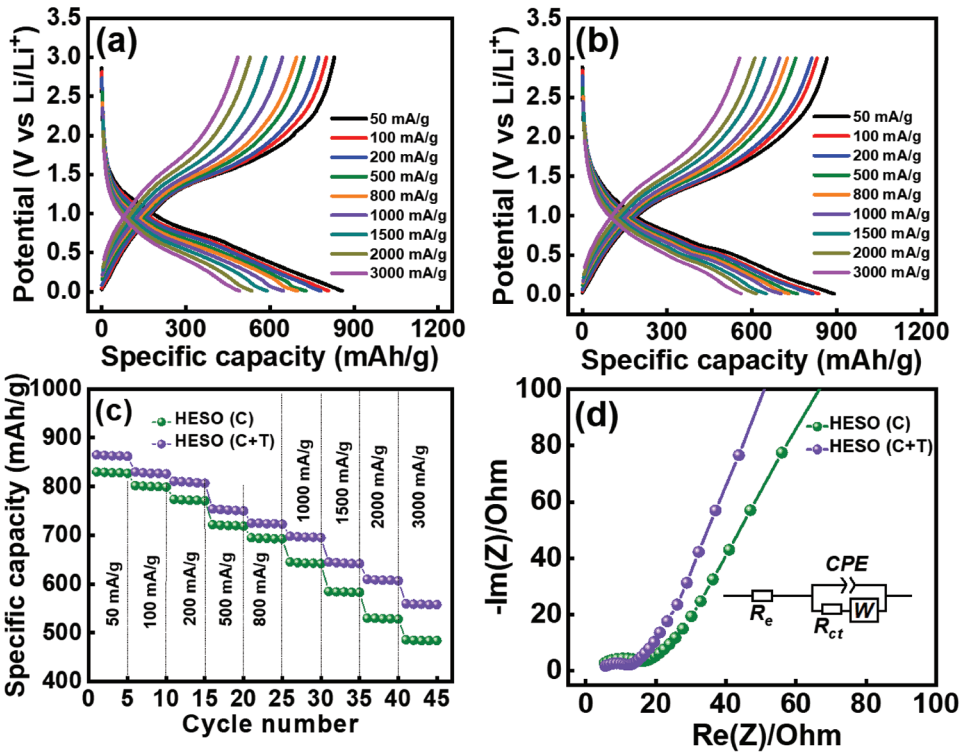

Figure 6. Charge–discharge curves of a) HESO (C) and b) HESO (C+T) electrodes measured at various rates. c) Comparative rate capability of various electrodes. d) EIS Nyquist spectra of various electrodes after five CV cycles.

The oxidation states of the electrode materials after cycling were examined via XPS (**Figure 8**). During the conversion process, irreversible reactions that leads to Cr, Mn, Fe, and Ni cation reduction and metallic Cr, Fe, and Ni formation, were identified. The Cr^{6+} disappears, giving Cr^0/Cr^{3+} ratios of 14.7/85.3 and 7.4/92.6 in HESO (C) and HESO (C+T), respectively. The concentration of Mn^{3+} in HESO (C) is largely reduced (to Mn^{2+}), from 59.6% in the pristine electrode to 27.4% after cycling. However, the reduction of Mn^{3+} to Mn^{2+} is notably less for HESO (C+T). The Mn^{2+}/Mn^{3+} ratio after cycling is 67.8/32.5 (compared to 62.5/37.5 before cycling). The ratios of $Fe^0/Fe^{2+}/Fe^{3+}$ are 16.6/47.2/36.4 and 15.8/44.6/39.6, while the $Ni^0/Ni^{2+}/Ni^{3+}$ ratios are 42/34.5/23.5 and 24.5/41.5/34 for HESO (C) and HESO (C+T), respectively. The Zn remains divalent in both electrodes. It is seen that the concentrations of metallic species in HESO (C) are higher than those in HESO (C+T).

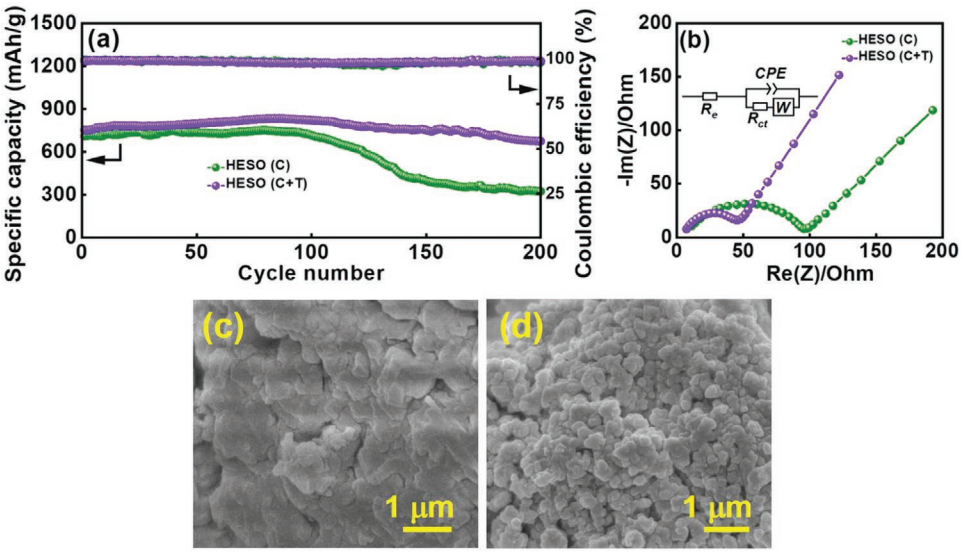

Figure 7. a) Cycling stability data of various electrodes measured at 500 mA g^{-1}. b) EIS Nyquist spectra of various electrodes after 200 cycles. SEM images of c) HESO (C) and d) HESO (C+T) electrodes after 200 cycles.

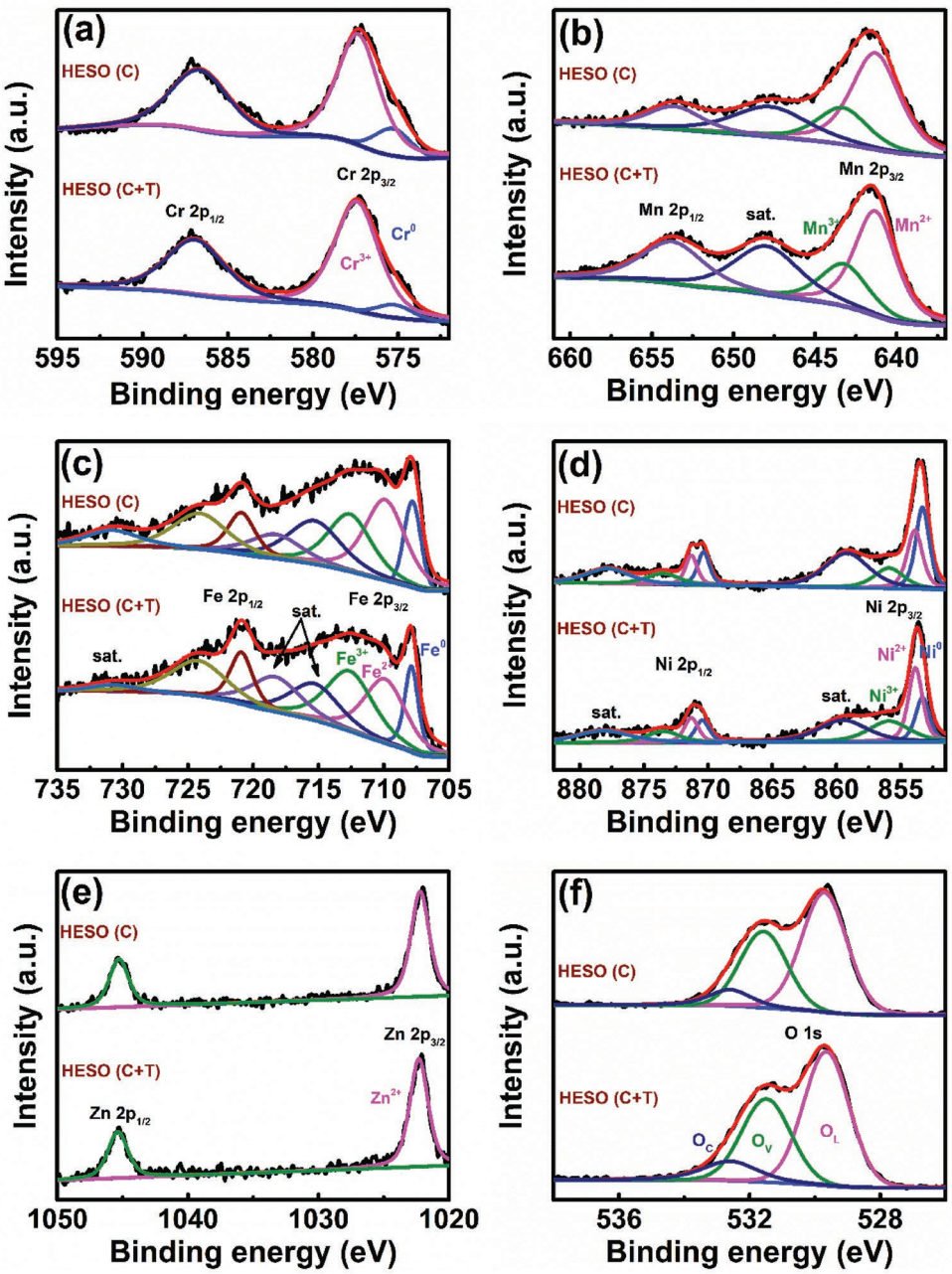

Figure 8. High-resolution XPS spectra of a) Cr 2p, b) Mn 2p, c) Fe 2p, d) Ni 2p, e) Zn 2p, and f) O 1s orbitals of HESO (C) and HESO (C+T) electrode after cycling.

The less cation irreversible reduction in the HESO (C+T) electrode explains the less capacity degradation upon cycling compared to the HESO (C) electrode. It was also found that the O_V content increases relatively less upon cycling for HESO (C+T) (Figure 8f versus Figure 5f), whereas the O_V content in HESO (C) substantially upsurges after the same cycle numbers, suggesting a remarkable phase transformation, which is examined using TEM analyses shown below.

The TEM image of HESO (C) after 200 cycles is shown in **Figure 9**a. The HRTEM image and SAED data indicate the transformation of the spinel phase to a rock-salt structure after cycling. Figure 9b shows *d*-spacings of 0.24 and 0.21 nm, corresponding to the (111) and (200) planes of the rock-salt structure (space group Fm-3m), respectively. The SAED pattern (Figure 9c) also supports the formation of rock-salt crystals. The diffraction rings are indexed to the (111), (200), and (220) crystalline planes. Figure 9e shows a TEM image of HESO (C+T) after cycling. The *d*-spacings of 0.50 nm in Figure 9f and 0.21 nm in Figure 9g belong to the (111) plane of the tetragonal spinel phase and (200) plane of the rock-salt phase, respectively. The SAED pattern (Figure 9h) shows the existence of both tetragonal spinel and rock-salt structures in the sample. After 200 cycles, both materials remained integrated, as confirmed by the EDS mapping data shown in

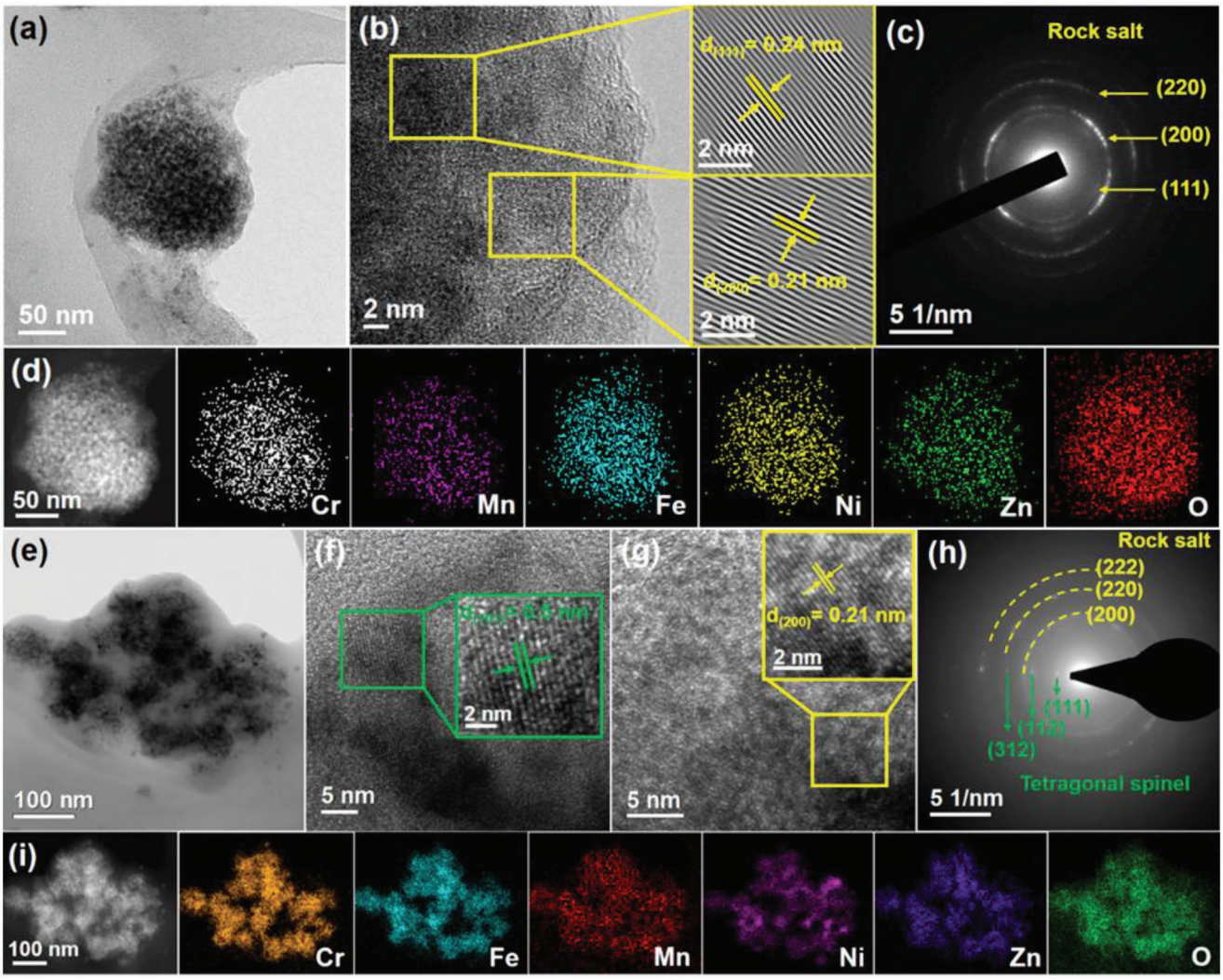

Figure 9. a) TEM and b) HRTEM images, c) SAED pattern, and d) STEM-EDS elemental mapping of HESO (C) after 200 cycles. e) TEM and f,g) HRTEM images, h) SAED pattern, and i) STEM-EDS elemental mapping of HESO (C+T) after 200 cycles.

Figure 9d,i. However, the cubic spinel phase in HESO (C) was completely converted to a rock-salt structure, whereas mixed tetragonal spinel and rock-salt phases were detected in HESO (C+T) after cycling. The lack of phase boundaries and less defects/oxygen vacancies in HESO (C) may decrease the redox reversibility during lithiation/delithiation. The formation of Li_2O and irreversible reduction of the constituent cations upon the conversion reaction inevitably led to the formation of the rock-salt phase, which is thermodynamically least stable according to Figure 4. In contrast, clearly higher reversibility of HESO (C+T) is confirmed since the tetragonal spinel phase is preserved after cycling. According to the DFT calculation results (Figure 4), the total convex hull energy of the mixed tetragonal spinel and rock-salt phases in HESO (C+T) composition can be considerably lower than that of the rock-salt structure in HESO (C) composition, indicating that the former electrode is more stable. This could be a cause for the less capacity fading of the HESO (C+T) electrode during the charge–discharge cycling (Figure 7a).

As explored by the high spatial-resolution EDS data and the XPS results in Figure 5b, the tetragonal domain (rather than the cubic domain) in HESO (C+T) is supposed to be Mn^{2+}-rich and thus O_V-rich. Accordingly, the tetragonal phase could facilitate the Li^+ transport and possess higher redox reversibility compared to the cubic phase. Therefore, the tetragonal phase can be preserved whereas the cubic structure is totally gone after cycling. Moreover, because some oxygen loss and/or Li trapping occurred after cycling, the electrode chemical composition can deviate from the initial composition that was used for the DFT calculation. This is probably another reason for that the cubic phase, the energetically preferred phase predicted in Figure 4 in an ideal case, did not actually appear in HESO (C+T) after cycling.

To evaluate the viability of the HESO (C+T) electrode for practical battery application, a HESO (C+T)||$LiNi_{0.8}Co_{0.1}Mn_{0.1}O_2$ full cell was assembled (**Figure 10**a). The obtained charge–discharge profiles measured at various C-rates are shown in Figure 10b (1 C = 275 mAh g^{-1} for the cathode). The specific

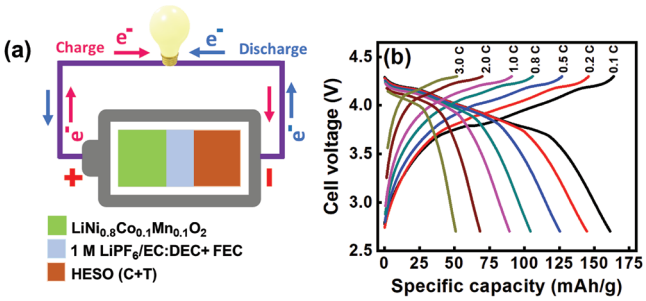

Figure 10. a) Scheme of LIB full cell with HESO (C+T) anode and $LiNi_{0.8}Co_{0.1}Mn_{0.1}O_2$ cathode. b) Charge–discharge profiles of HESO (C+T)|| $LiNi_{0.8}Co_{0.1}Mn_{0.1}O_2$ full cell measured at various rates.

capacities were calculated based on the total mass of anode and cathode active materials. Accordingly, the energy density of the full cell (@0.1 C mA g^{-1}) is estimated to be ≈610 Wh kg^{-1} (based on electrode materials), which shows the great potential of the proposed HESO (C+T) for use in LIBs.

3. Conclusion

Typically, "pure phase" HEO anode is thought to be essential to give good electrochemical performance of LIBs. However, we report here that this is not a necessary condition and a proper secondary phase is actually advantageous. Two kinds of Co-free HESO, containing Cr, Mn, Fe, Ni, and Zn, were synthesized, resulting in HESO (C) and HESO (C+T) with distinct crystallinities. The secondary tetragonal spinel phase in HESO (C+T) introduces phase boundaries and extra defects/oxygen vacancies, which improve the redox kinetics and electroactivity during the lithiation/delithiation reactions. The reduced R_{ct} and enhanced D_{Li^+} contributed to the superior first-cycle CE, specific capacity, and rate capability of the HESO (C+T) electrode. In addition, these heterogeneous (or defective) sites promote phase change reversibility and reduce the lattice stress during charging/discharging. After cycling, the tetragonal phase was preserved, and the morphology deterioration was less for the HESO (C+T) electrode, resulting in its significantly improved cyclability. The HESO (C+T) electrode having a high capacity of 865 mAh g^{-1} was paired with a $LiNi_{0.8}Co_{0.1}Mn_{0.1}O_2$ positive electrode to form a full cell, which showed an attractive gravimetric energy density of ≈610 Wh kg^{-1} (based on electrode-active material weight). The "secondary phase" material design strategy developed in the present work launches a new route to further advance the charge–discharge performance of HEO electrodes for better LIBs in the future.

4. Experimental Section

Material Synthesis: $Cr(NO_3)_3{\cdot}9H_2O$ (Alfa Aesar, 98.5%), $Mn(NO_3)_2{\cdot}6H_2O$ (Alfa Aesar, 98.5%), $Fe(NO_3)_3{\cdot}9H_2O$ (J.T. Baker, 99%), $Ni(NO_3)_2{\cdot}6H_2O$ (Alfa Aesar, 98.5%), and $Zn(NO_3)_2{\cdot}6H_2O$ (Alfa Aesar, 98.5%) were used as the metal precursors. In the solvothermal approach, equimolar precursors were mixed in a solution consisting of 40 ml ethylene glycol and 10 mmol sodium acetate under stirring for 1 h. Afterward, the solution was poured into a Teflon-lined stainless-steel autoclave and heated at 200 °C for 16 h. After cooling down to room temperature, the solution was centrifuged and rinsed with ethanol and de-ionized (DI) water several times. Subsequently, the solution was filtered to obtain the powdery product, which was then dried in a vacuum oven at 60 °C for 12 h. The resulting powder was heated at various temperatures for 2 h with a ramp rate of 5 °C min^{-1}. The obtained sample was designated as HESO (C). In the hydrothermal process, the same equimolar precursors were mixed in a solution consisting of 40 ml DI water and (1-hexadecyl)trimethylammonium bromide (CTAB, Alfa Aesar, 98.5%). Afterward, urea (urea/total metal precursors = 6/1, in a molar ratio) was added to the solution. The obtained solution was then poured into a Teflon-lined stainless-steel autoclave and heated at 140 °C for 5 h. The same procedures to those for HESO (C) were then carried out to obtain a powdery sample, which is designated as HESO (C+T).

Material Characterizations: The crystalline structures of the samples were examined using XRD (Bruker D8 Discover) with Cu K_α radiation (λ = 0.15418 nm). The surface morphology was examined using SEM (JOEL 6701F). HRTEM (Tecnai F20 G2) and (SAED) were used to study the microstructures. STEM-EDS mapping was conducted to probe the elemental distribution. EELS (JEOL JEM-2100F Cs STEM) analysis was conducted to examine the valence state evolution of Cr, Mn, Fe, and Ni after the first lithiation-delithiation cycle. The HESO composition was determined using ICP-MS (Thermo Element XR). The surface chemistry was analyzed using XPS (PHI 5000). EPR (Bruker, ELEXSYS E580) analysis was conducted to investigate the Ov content.

Electrode Preparation: The electrode slurry was composed of 80 wt.% HESO, 10 wt.% Super P, and 10 wt.% sodium polyacrylate binder in deionized water. The slurry was cast onto 8-µm-thick Cu foil with a doctor blade and vacuum-dried at 90 °C for 6 h. The obtained electrode coating was roll-pressed and punched to match the required dimensions of a CR2032 coin cell. The HESO loading was ≈2.0 mg cm^{-2}. Li foil and a glass fiber membrane were used as the counter electrode and separator, respectively. 70 µL of the electrolyte (1 M lithium hexafluorophosphate in ethylene carbonate/diethyl carbonate (1:1 by volume) mixed solvent with 5 wt.% fluoroethylene carbonate additive) was used in each cell. The coin cells were assembled in an Ar-filled glove box (Vigor Tech. Co. Ltd.), where both the oxygen and moisture content levels were maintained at below 0.2 ppm.

Electrochemical Measurements: CV measurement was performed within a range of 0.01–3.0 V (versus Li/Li^+) with a potential sweep rate of 0.1 mV s^{-1}. EIS tests were carried out using a BioLogic VSP-300 workstation in a frequency range of 10^6–10^{-2} Hz with a perturbation amplitude of 10 mV. The cell charge–discharge properties (such as capacity, rate capability, and cycling stability) were evaluated using a NEWARE CT-4000 battery tester at 25 °C. For every condition, at least five parallel cells were tested. The performance deviation was typically within ≈3%; the reported capacities are the median values. GITTwas performed to determine the Li^+ diffusion coefficients in the electrodes. GITT was tested at a current density of 100 mA g^{-1} over a potential range of 0.01–3.0 V. Postmortem SEM and TEM characterizations were performed to check the morphological integrity and structural variations of the electrodes after 200 charge–discharge cycles. The cycled electrodes after lithiation were taken out from the cells inside the glove box, washed with dimethyl carbonate solvent, and then dried prior to various analyses. For construction of a HESO (C+T)||$LiNi_{0.8}Co_{0.1}Mn_{0.1}O_2$ full cell, an anode-to-cathode capacity ratio of 1.2 was used. The HESO (C+T) anode was preconditioned and lithiated by 20% in a half cell prior to the full cell assembly.

Computational Method: The HESO (C) and HESO (C+T) materials were modelled by 2 × 2 × 2 primitive cells of cubic spinel, tetragonal spinel, and rock-salt structures based on the lattice constants measured by XRD. Based on the ICP-MS data, the chemical compositions of the two samples, assumed having a spinel structure, were set as $Zn_{10}Mn_4Fe_{12}Ni_{12}Cr_{10}O_{64}$ and $Zn_9Mn_9Fe_9Ni_{10}Cr_{11}O_{64}$, respectively. For a rock-salt structure, they were set as $Zn_6Mn_3Fe_8Ni_8Cr_7O_{32}$ and $Zn_6Mn_6Fe_6Ni_7Cr_7O_{32}$, respectively. The cations were swapped by ChemDash after 100 steps of basin-hoping DFT calculation to reach an energetic global minimum configuration.[62]The DFT calculation

was done by the Vienna Ab initio Simulation Package (VASP) with the projected augmented wave (PAW) potentials for core electrons.[63,64] The valence space for Zn, Mn, Fe, Ni, Cr, and O atoms consisted of 12, 13, 14, 16, 12, and 6 electrons, respectively. All the structure optimizations were done by Perdew-Burke-Ernzerhof (PBE) functional with spin-polarized generalized gradient approximations (GGA)+U correction.[65] The U value followed previous research (Mn: 3.9 eV, Fe: 5.3 eV, Ni: 6.2 eV, Cr: 3.7 eV).[66,67] The energy cut-off was set at 400 eV with a gamma-only k-point space for the spinel structure and $2 \times 2 \times 2$ k mesh for the rock-salt structure. All the forces acting on the ions were below 0.02 eV $Å^{-1}$ after relaxation. More accurate energies of the best structures were then calculated by the input consisting of the entries on Materials Project to construct a 6D phase diagram.[66–68] The energy per atom above the convex hull was worked out to determine the stability of the above structures.

Statistical Analysis: The charge–discharge experiments of the HESO electrodes were repeated at least five times to ensure validity. The reported capacities are the mean values, and the relative standard deviation is within 3%. The XPS data fitting was done using XPSPEAK 4.1 software. All the XPS spectra were calibrated with the binding energy of C 1s at 284.8 eV. The Origin software was used for data analysis and processing. The DFT calculation was done by the Vienna Ab initio Simulation Package with the projected augmented wave potentials for core electrons. All the structure optimizations were done by Perdew-Burke-Ernzerhof functional with spin-polarized generalized gradient approximations +U correction.

Supporting Information

Supporting Information is available from the Wiley Online Library or from the author.

Acknowledgements

T.X.N. and J.P. contributed equally to this work. The financial support provided for this work by the National Science and Technology Council of Taiwan is gratefully appreciated. The computational resources were supported by TAIWANIA at the National Center for High-Performance Computing (NCHC) of National Applied Research Laboratories (NARLabs) in Taiwan. The use of [EM000800] JEOL JEM-2100F Cs STEM in the Core Facility Center of National Cheng Kung University is acknowledged.

Conflict of Interest

The authors declare no conflict of interest.

Data Availability Statement

The data that support the findings of this study are available from the corresponding author upon reasonable request.

Keywords

Co-free electrodes, high entropy stabilization, hydrothermal process, secondary phase, solvothermal process

Received: January 13, 2023
Revised: March 10, 2023
Published online:

[1] M. Z. Jacobson, *Energy Environ. Sci.* **2009**, *2*, 148.
[2] N. Nitta, F. Wu, J. T. Lee, G. Yushin, *Mater. Today* **2015**, *18*, 252.
[3] S. Chu, Y. Cui, N. Liu, *Nat. Mater.* **2017**, *16*, 16.
[4] J. Asenbauer, T. Eisenmann, M. Kuenzel, A. Kazzazi, Z. Chen, D. Bresser, *Sustainable Energy Fuels* **2020**, *4*, 5387.
[5] P. Poizot, S. Laruelle, S. Grugeon, L. Dupont, J. Tarascon, *Nature* **2000**, *407*, 496.
[6] J. Cabana, L. Monconduit, D. Larcher, M. R. Palacin, *Adv. Mater.* **2010**, *22*, E170.
[7] C. Duan, K. Tian, X. Li, D. Wang, H. Sun, R. Zheng, Z. Wang, Y. Liu, *Ceram. Int.* **2021**, *47*, 32025.
[8] D. S. McClure, *J. Phys. Chem. Solids* **1957**, *3*, 311.
[9] R. Zhang, Q. Yuan, R. Ma, X. Liu, C. Gao, M. Liu, C.-L. Jia, H. Wang, *RSC Adv.* **2017**, *7*, 21926.
[10] L. Plyasova, T. Minyukova, T. Yurieva, E. Uyanga, I. Bobrikov, V. Zaikovskii, A. Balagurov, *Mater. Chem. Phys.* **2018**, *211*, 278.
[11] M. Sanad, A. K. Yousef, M. Rashad, A. Naggar, A. El-Sayed, *Phys. B* **2020**, *579*, 411889.
[12] K. Cao, T. Jin, L. Yang, L. Jiao, *Mater. Chem. Front.* **2017**, *1*, 2213.
[13] C. Oses, C. Toher, S. Curtarolo, *Nat. Rev. Mater.* **2020**, *5*, 295.
[14] M. Fu, X. Ma, K. Zhao, X. Li, D. Su, *Iscience* **2021**, *24*, 102177.
[15] A. Sarkar, Q. Wang, A. Schiele, M. R. Chellali, S. S. Bhattacharya, D. Wang, T. Brezesinski, H. Hahn, L. Velasco, B. Breitung, *Adv. Mater.* **2019**, *31*, 1806236.
[16] C.-Y. Huang, C.-W. Huang, M.-C. Wu, J. Patra, T. X. Nguyen, M.-T. Chang, O. Clemens, J.-M. Ting, J. Li, J.-K. Chang, *Chem. Eng. J.* **2021**, *420*, 129838.
[17] X. F. Luo, J. Patra, W. T. Chuang, T. X. Nguyen, J. M. Ting, J. Li, C. W. Pao, J. K. Chang, *Adv. Sci.* **2022**, *9*, 2201219.
[18] D. Wang, S. Jiang, C. Duan, J. Mao, Y. Dong, K. Dong, Z. Wang, S. Luo, Y. Liu, X. Qi, *J. Alloys Compd.* **2020**, *844*, 156158.
[19] K. Tian, H. He, X. Li, D. Wang, Z. Wang, R. Zheng, H. Sun, Y. Liu, Q. Wang, *J. Mater. Chem. A* **2022**, *10*, 14943.
[20] K.-H. Tian, C.-Q. Duan, Q. Ma, X.-L. Li, Z.-Y. Wang, H.-Y. Sun, S.-H. Luo, D. Wang, Y.-G. Liu, *Rare Met.* **2022**, *41*, 1265.
[21] A. Sarkar, L. Velasco, D. Wang, Q. Wang, G. Talasila, L. de Biasi, C. Kübel, T. Brezesinski, S. S. Bhattacharya, H. Hahn, B. Breitung, *Nat. Commun.* **2018**, *9*, 3400.
[22] N. Qiu, H. Chen, Z. Yang, S. Sun, Y. Wang, Y. Cui, *J. Alloys Compd.* **2019**, *777*, 767.
[23] T. X. Nguyen, J. Patra, J.-K. Chang, J.-M. Ting, *J. Mater. Chem. A* **2020**, *8*, 18963.
[24] Y.-M. Kang, M.-S. Song, J.-H. Kim, H.-S. Kim, M.-S. Park, J.-Y. Lee, H.-K. Liu, S. Dou, *Electrochim. Acta* **2005**, *50*, 3667.
[25] L.-H. Wang, X.-L. Teng, Y.-F. Qin, Q. Li, *Ceram. Int.* **2021**, *47*, 5739.
[26] J. Patra, T. X. Nguyen, C. C. Tsai, O. Clemens, J. Li, P. Pal, W. K. Chan, C. H. Lee, H. Y. T. Chen, J. M. Ting, *Adv. Funct. Mater.* **2022**, *32*, 2110992.
[27] T. X. Nguyen, C.-C. Tsai, J. Patra, O. Clemens, J.-K. Chang, J.-M. Ting, *Chem. Eng. J.* **2022**, *430*, 132658.
[28] H. Chen, N. Qiu, B. Wu, Z. Yang, S. Sun, Y. Wang, *RSC Adv.* **2020**, *10*, 9736.
[29] B. Xiao, G. Wu, T. Wang, Z. Wei, Y. Sui, B. Shen, J. Qi, F. Wei, Q. Meng, Y. Ren, *Ceram. Int.* **2021**, *47*, 33972.
[30] L. Lin, K. Wang, A. Sarkar, C. Njel, G. Karkera, Q. Wang, R. Azmi, M. Fichtner, H. Hahn, S. Schweidler, B. Breitung, *Adv. Energy Mater.* **2022**, *12*, 2103090.
[31] G. Chen, C. Li, H. Li, L. Wang, K. Chen, L. An, *J. Eur. Ceram. Soc.* **2021**, *41*, 309.
[32] N. Um, T. Hirato, *Hydrometallurgy* **2014**, *146*, 142.
[33] B. Bao, J. Liu, H. Xu, B. Liu, K. Zhang, Z. Jin, *RSC Adv.* **2017**, *7*, 8589.
[34] J. Zhang, R. Chu, Y. Chen, Y. Zeng, Y. Zhang, H. Guo, *Electrochim. Acta* **2019**, *319*, 518.
[35] A. Aoki, *Jpn. J. Appl. Phys.* **1976**, *15*, 305.
[36] Y. Umezawa, C. N. Reilley, *Anal. Chem.* **1978**, *50*, 1290.

[37] Z. Chen, J. Wang, D. Chao, T. Baikie, L. Bai, S. Chen, Y. Zhao, T. C. Sum, J. Lin, Z. Shen, *Sci. Rep.* **2016**, *6*, 25771.
[38] A. Grosvenor, B. Kobe, M. Biesinger, N. McIntyre, *Surf. Interface Anal.* **2004**, *36*, 1564.
[39] K. Lian, D. Kirk, S. Thorpe, *J. Electrochem. Soc.* **1995**, *142*, 3704.
[40] A. Mansour, *Surf. Sci. Spectra* **1994**, *3*, 231.
[41] J. H. Kim, Y. J. Jang, J. H. Kim, J.-W. Jang, S. H. Choi, J. S. Lee, *Nanoscale* **2015**, *7*, 19144.
[42] X. Liu, Y. Xing, K. Xu, H. Zhang, M. Gong, Q. Jia, S. Zhang, W. Lei, *Small* **2022**, *18*, 2200524.
[43] J. Zhao, X. Yang, Y. Huang, F. Du, Y. Zeng, *ACS Appl. Mater. Interfaces* **2021**, *13*, 58674.
[44] P. Ghigna, L. Airoldi, M. Fracchia, D. Callegari, U. Anselmi-Tamburini, P. D'angelo, N. Pianta, R. Ruffo, G. Cibin, D. O. de Souza, *ACS Appl. Mater. Interfaces* **2020**, *12*, 50344.
[45] H.-Z. Xiang, H.-X. Xie, Y.-X. Chen, H. Zhang, A. Mao, C.-H. Zheng, *J. Mater. Sci.* **2021**, *56*, 8127.
[46] D. Puthusseri, M. Wahid, S. Ogale, *ACS Omega* **2018**, *3*, 4591.
[47] Q. Xia, M. Avdeev, S. Schmid, H. Liu, B. Johannessen, C. D. Ling, *Batteries Supercaps* **2021**, *4*, 195.
[48] J.-M. Tarascon, M. Armand, *Materials for Sustainable Energy: A Collection of Peer-Reviewed Research and Review Articles from Nature Publishing Group* (Ed: V. Dusastre), World Scientific Publishing, Singapore **2011**, p. 171.
[49] Y. Lu, L. Yu, X. W. D. Lou, *Chem* **2018**, *4*, 972.
[50] S. H. Yu, S. H. Lee, D. J. Lee, Y. E. Sung, T. Hyeon, *Small* **2016**, *12*, 2146.
[51] H. Chen, N. Qiu, B. Wu, Z. Yang, S. Sun, Y. Wang, *RSC Adv.* **2019**, *9*, 28908.
[52] E. Lokcu, C. Toparli, M. Anik, *ACS Appl. Mater. Interfaces* **2020**, *12*, 23860.
[53] Y. Zheng, X. Wu, X. Lan, R. Hu, *Processes* **2021**, *10*, 49.
[54] H. Guo, J. Shen, T. Wang, C. Cheng, H. Yao, X. Han, Q. Zheng, *Ceram. Int.* **2022**, *48*, 3344.
[55] J. Wei, K. Rong, X. Li, Y. Wang, Z.-A. Qiao, Y. Fang, S. Dong, *Nano Res.* **2022**, *15*, 2756.
[56] J. Patra, H.-T. Huang, W. Xue, C. Wang, A. S. Helal, J. Li, J.-K. Chang, *Energy Storage Mater.* **2019**, *20*, 470.
[57] J. Patra, P. C. Rath, C. Li, H. M. Kao, F. M. Wang, J. Li, J. K. Chang, *ChemSusChem* **2018**, *11*, 3923.
[58] J. Patra, S.-C. Wu, I.-C. Leu, C.-C. Yang, R. S. Dhaka, S. Okada, H.-L. Yeh, C.-M. Hsieh, B. K. Chang, J.-K. Chang, *ACS Appl. Energy Mater.* **2021**, *4*, 5738.
[59] Y. Zou, W. Zhang, N. Chen, S. Chen, W. Xu, R. Cai, C. L. Brown, D. Yang, X. Yao, *ACS Nano* **2019**, *13*, 12259.
[60] Q. Li, D. Ning, D. Zhou, K. An, D. Wong, L. Zhang, Z. Chen, G. Schuck, C. Schulz, Z. Xu, *J. Mater. Chem. A* **2020**, *8*, 7733.
[61] W. Ma, C. Zhang, C. Liu, X. Nan, H. Fu, G. Cao, *ACS Appl. Mater. Interfaces* **2016**, *8*, 19542.
[62] P. M. Sharp, M. S. Dyer, G. R. Darling, J. B. Claridge, M. J. Rosseinsky, *Phys. Chem. Chem. Phys.* **2020**, *22*, 18205.
[63] G. Kresse, J. Hafner, *Phys. Rev. B* **1993**, *47*, 558.
[64] G. Kresse, D. Joubert, *Phys. Rev. B* **1999**, *59*, 1758.
[65] J. P. Perdew, K. Burke, M. Ernzerhof, *Phys. Rev. Lett.* **1996**, *77*, 3865.
[66] A. Jain, G. Hautier, C. J. Moore, S. P. Ong, C. C. Fischer, T. Mueller, K. A. Persson, G. Ceder, *Comput. Mater. Sci.* **2011**, *50*, 2295.
[67] A. Jain, G. Hautier, S. P. Ong, C. J. Moore, C. C. Fischer, K. A. Persson, G. Ceder, *Phys. Rev. B* **2011**, *84*, 045115.
[68] A. Jain, S. P. Ong, G. Hautier, W. Chen, W. D. Richards, S. Dacek, S. Cholia, D. Gunter, D. Skinner, G. Ceder, *APL Mater.* **2013**, *1*, 011002.

ADVANCED FUNCTIONAL MATERIALS

Supporting Information

for *Adv. Funct. Mater.,* DOI: 10.1002/adfm.202300509

Secondary-Phase-Induced Charge–Discharge Performance Enhancement of Co-Free High Entropy Spinel Oxide Electrodes for Li-Ion Batteries

Thi Xuyen Nguyen, Jagabandhu Patra, Chia-Chien Tsai, Wen-Ye Xuan, Hsin-Yi Tiffany Chen, Matthew S. Dyer, Oliver Clemens, Ju Li, Subhasish Basu Majumder, Jeng-Kuei Chang, and Jyh-Ming Ting**

Supporting Information

Secondary-phase-induced charge-discharge performance enhancement of Co-free high entropy spinel oxide electrodes for Li-ion batteries

Thi Xuyen Nguyen[#], Jagabandhu Patra[#], Chia-Chien Tsai[#], Wen-Ye Xuan, Hsin-Yi Tiffany Chen, Matthew S. Dyer, Oliver Clemens, Ju Li, Subhasish Basu Majumder, Jeng-Kuei Chang, Jyh-Ming Ting**

The methodology to determine the high entropy material configurations

The high entropy material configuration was generated through an energy global minimal search using the basin hopping method[1] implemented in the crystal structure prediction code ChemDASH (Chemically Directed Atom Swap Hopping).[2] In the basin hopping calculation, the beginning configuration was generated by randomly placing the metal atoms at different sites. We then swapped the atoms at chemical unfavorable sites determined by the chemical bonding length and valence numbers.[3] If the newly generated configuration has a lower energy or the Boltzmann factor is lower than a random number, we accepted the swap. After generating 100 models through the basin hopping calculations, we took the crystal structure with the lowest energy as a representative model.

After getting the lowest energy configurations for the three crystal structures (cubic spinel, tetragonal spinel, and rock salt) in both elements ratio (600 models were tested in total), to compare the stability of configurations with different ratios of elements, we employed the convex hull energy with a benchmark of the crystal structures containing the same elements in the Materials Project database.[4] The boundary of the convex hull was determined using the phase diagram method implemented in Python Materials Genomics (pymatgen).[5]

References

[1]D. J. Wales, J. P. Doye, *The Journal of Physical Chemistry A* **1997**, *101*, 5111.

[2]P. M. Sharp, M. S. Dyer, G. R. Darling, J. B. Claridge, M. J. Rosseinsky, *Phys. Chem. Chem. Phys.* **2020**, *22*, 18205.

[3]I. D. Brown, *The chemical bond in inorganic chemistry: the bond valence model*, *Vol. 27*, Oxford university press, **2016**.

[4]A. Jain, S. P. Ong, G. Hautier, W. Chen, W. D. Richards, S. Dacek, S. Cholia, D. Gunter, D. Skinner, G. Ceder, *APL Mater.* **2013**, *1*, 011002.

[5]S. P. Ong, W. D. Richards, A. Jain, G. Hautier, M. Kocher, S. Cholia, D. Gunter, V. L. Chevrier, K. A. Persson, G. Ceder, *Comput. Mater. Sci.* **2013**, *68*, 314.

Table S1. Rietveld refinement data for HESO (C).

Sample ID			HESO (C)			
Phase			Cubic spinel			
R-Bragg			3.732			
Space-group			Fd-3m			
Wt% - Rietveld			100 %			
Cell volume ($Å^3$)			579.8(2)			
Crystal Density (g cm^{-3})			5.423(2)			
Lattice parameter (Å)			8.3384(10)			
Label	Wyckoff site	x	y	z	Atom	Occupation
Anion	32e	0.3785(4)	0.3785(4)	0.3785(4)	O	1
Oct.	16c	0.625	0.625	0.625	Cr	0.2162
					Mn	0.0914
					Fe	0.2472
					Ni	0.2436
					Zn	0.2016
Tetr.	8b	0	0	0	Cr	0.2162
					Mn	0.0914
					Fe	0.2472
					Ni	0.2436
					Zn	0.2016

Table S2. Rietveld refinement data for cubic spinel phase in HESO (C+T).

Sample ID			HESO (C+T)			
Phase			Cubic spinel			
R-Bragg			3.728			
Space-group			Fd-3m			
Wt% - Rietveld			88%			
Cell volume ($Å^3$)			578.85(16)			
Crystal Density (g cm^{-3})			5.4150(15)			
Lattice parameter (Å)			8.3340(8)			
Label	Wyckoff site	x	y	z	Atom	Occupation
Anion	32e	0.3785(6)	0.3785(6)	0.3785(6)	O	1
Oct.	16c	0.625	0.625	0.625	Cr	0.2189
					Mn	0.1865
					Fe	0.1823
					Ni	0.2172
					Zn	0.1951
Tetr.	8b	0	0	0	Cr	0.2189
					Mn	0.1865
					Fe	0.1823
					Ni	0.2172
					Zn	0.1951

Table S3. Rietveld refinement data for tetragonal spinel phase in HESO (C+T).

Sample ID			HESO (C+T)			
Phase			Tetragonal spinel			
R-Bragg			2.532			
Space-group			I41/amd			
Wt% - Rietveld			12.0%			
Cell volume ($Å^3$)			304.52(18)			
Crystal Density (g cm^{-3})			4.991(3)			
Lattice parameter (Å)			a=5.7296(13) c=9.276(3)			
Label	Wyckoff site	x	y	z	Atom	Occupation
Anion	32e	0.3785(6)	0.3785(6)	0.3785(6)	O	1
Oct.	16c	0.625	0.625	0.625	Cr	0.2189
					Mn	0.1865
					Fe	0.1823
					Ni	0.2172
					Zn	0.1951
Tetr.	8b	0	0	0	Cr	0.2189
					Mn	0.1865
					Fe	0.1823
					Ni	0.2172
					Zn	0.1951

Table S4. Chemcial compositions (evaluated using high spatial-resolution EDS) and calculated entropy values of cubic and tetragonal phases in HESO (C+T).

Element	Cubic phase	Tetragonal phase
O	61.3%	59.2%
Cr	10.4%	8.3%
Mn	3.7%	8.7%
Fe	9.7%	9.2%
Ni	7.4%	6.5%
Zn	7.5%	8.1%
Total	100%	100%
ΔS	1.56 R	1.60 R

Table S5. Chemical compositions of HESO (C) and HESO (C+T) measured using ICP-MS.

Sample	Cr (at.%)	Mn (at.%)	Fe (at.%)	Ni (at.%)	Zn (at.%)	ΔS
HESO (C)	24.6	9.1	24.7	21.4	20.2	1.56R
HESO (C+T)	21.9	18.7	18.2	21.7	19.5	1.61R

Table S6. Comparison of capacities, rate capability, and cycling stability of HESO (C+T) and various HEO electrodes reported in the literature.

Material	Low-rate performance	High-rate performance	Cycling stability	Ref.
$(Co_{0.2}Cu_{0.2}Mg_{0.2}Ni_{0.2}Zn_{0.2})O$	~600 mAh g^{-1} @ 50 mAg^{-1}	~160 mAh g^{-1} @ 3000 mAg^{-1}	100% after 300 cycles @ 200 mAg^{-1}	1
$Mg_{0.2}Co_{0.2}Ni_{0.2}Cu_{0.2}Zn_{0.2}O$	955 mAh g^{-1} @ 100 mAg^{-1}	490 mAh g^{-1} @ 3000 mAg^{-1}	100% after 300 cycles @ 100 mAg^{-1}	2
$(Mg_{0.2}Co_{0.2}Ni_{0.2}Cu_{0.2}Zn_{0.2})O$	829 mAh g^{-1} @ 100 mAg^{-1}	408 mAh g^{-1} @ 2000 mAg^{-1}	~100% after 150 cycles @ 200 mAg^{-1}	3
$(MgCoNiZn)_{0.65}Li_{0.35}O$	925 mAh g^{-1} @ 100 mAg^{-1}	610 mAh g^{-1} @ 1000 mAg^{-1}	~85% after 100 cycles @ 1000 mAg^{-1}	4
$Mg_{0.2}Co_{0.2}Ni_{0.2}Cu_{0.2}Zn_{0.2}O$	~600 mAh g^{-1} @ 89 mAg^{-1}	~300 mAh g^{-1} @ 1800 mAg^{-1}	NA	5
$(Ni_{0.2}Co_{0.2}Mn_{0.2}Fe_{0.2}Ti_{0.2})_3O_4$	594 mAh g^{-1} @ 50 mAg^{-1}	343 mAh g^{-1} @ 2500 mAg^{-1}	~100% after 100 cycles @ 100 mAg^{-1}	6
$(CoCrMnFeNi)_3O_4$	1235 mAh g^{-1} @ 20 mAg^{-1}	500 mAh g^{-1} @ 2000 mAg^{-1}	90% after 200 cycles @ 500 mA hg^{-1}	7
$(FeCoNiCrMn)_3O_4$	735 mAh g^{-1} @ 50 mAg^{-1}	180 mAh g^{-1} @ 2000 mAg^{-1}	~80% after 300 cycles @ 50 mAg^{-1}	8
$(FeCoNiCrMnZnLi)_3O_4$	695 mAh g^{-1} @ 50 mAg^{-1}	173 mAh g^{-1} @ 2000 mAg^{-1}	~80% after 100 cycles @ 500 mAg^{-1}	9
$(Al_{0.2}CoCrFeMnNi)_{0.58}O_{4-\delta}$	~1400 mAh g^{-1} @ 100 mAg^{-1}	634 mAh g^{-1} @ 3000 mAg^{-1}	~40% after 500 cycles @ 200 mAg^{-1}	10
$(MgCuNiCoZn)O$	~400 mAh g^{-1} @ 100 mAg^{-1}	250 mAh g^{-1} @ 5000 mAg^{-1}	~100% after 1000 cycles @ 200 mAg^{-1}	11
$(CoCuMgNiZn)O$	477 mAh g^{-1} @ 100 mAg^{-1}	240 mAh g^{-1} @ 2000 mAg^{-1}	92% after 200 cycles @ 120 mAg^{-1}	12
$(CoCrMnFeNi)_3O_4$	1225 mAh g^{-1} @ 20 mAg^{-1}	485 mAh g^{-1} @ 2000 mAg^{-1}	91% after 200 cycles @ 500 mAg^{-1}	13
$(Co_{0.2}Cr_{0.2}Fe_{0.2}Mn_{0.2}Ni_{0.2})_3O_4$	~863 mAh g^{-1} @ 100 mAg^{-1}	~428 mAh g^{-1} @ 10000 mAg^{-1}	100% after 50 cycles @ 100 mAg^{-1}	14
$(FeNiCrMnZn)_3O_4$	692 mAh g^{-1} @ 100 mAg^{-1}	260 mAh g^{-1} @ 3000 mAg^{-1}	~85% after 100 cycles @ 500 mAg^{-1}	15
$(Mg_{0.2}Ti_{0.2}Zn_{0.2}Cu_{0.2}Fe_{0.2})_3O_4$	571 mAh g^{-1} @ 100 mAg^{-1}	268 mAh g^{-1} @ 2000 mAg^{-1}	~87% after 300 cycles @ 100 mAg^{-1}	16
$(CrMnFeNiCu)_3O_4$	755 mAh g^{-1} @ 50 mAg^{-1}	451 mAh g^{-1} @ 2000 mAg^{-1}	99% after 250 cycles @ 500 mAg^{-1}	17
$(CrMnFeNiCu)_3O_4$	800 mAh g^{-1} @ 50 mAg^{-1}	480 mAh g^{-1} @ 2000 mAg^{-1}	100% after 400 cycles @ 500 mAg^{-1}	18
$(Mg_{0.2}Cr_{0.2}Fe_{0.2}Mn_{0.2}Co_{0.2})_3O_4$	~990 mAh g^{-1} @ 100 mAg^{-1}	~380 mAh g^{-1} @ 5000 mAg^{-1}	100% after 1000 cycles @ 1000 mAg^{-1}	19
$Mg_{0.05}Cr_{0.21}Ni_{0.22}Cu_{0.28}Zn_{0.24})_3O_4$ @PANI	~800 mAh g^{-1} @ 100 mAg^{-1}	598 mAh g^{-1} @ 2000 mAg^{-1}	55% after 3200 cycles @ 4000 mAg^{-1}	20
$(FeNiCrMnMgAl)_3O_4$	~520 mAh g^{-1} @ 100 mAg^{-1}	350 mAh g^{-1} @ 4000 mAg^{-1}	99.8% after 200 cycles @ 200 mAg^{-1}	21
$(FeCoNiCrMn)_3O_4$	~967 mAh g^{-1} @ 100 mAg^{-1}	483 mAh g^{-1} @ 3000 mAg^{-1}	86.2% after 1200 cycles @ 2000 mAg^{-1}	22

$(Mg_{0.2}Co_{0.2}Ni_{0.2}Cu_{0.2}Zn_{0.2})O$@graphene	~1001 mAh g^{-1} @ 100 mAg^{-1}	393 mAh g^{-1} @ 2000 mAg^{-1}	95% after 200 cycles @ 100 mAg^{-1}	23
$Zn_{0.5}Co_{0.5}Mn_{0.5}Fe_{0.5}Al_{0.5}Mg_{0.5}O_4$	~600 mAh g^{-1} @ 500 mAg^{-1}	290 mAh g^{-1} @ 5000 mAg^{-1}	81% after 5000 cycles @ 2000 mAg^{-1}	24
$(CrMnFeNiZn)_3O_4$ [HESO (C+T)]	865 mAh g^{-1} @ 50 mAg^{-1}	560 mAh g^{-1} @ 3000 mAg^{-1}	90% after 200 cycles @ 500 mAg^{-1}	This work

References

1. A. Sarkar, L. Velasco, D. Wang, Q. Wang, G. Talasila, L. de Biasi, C. Kübel, T. Brezesinski, S. S. Bhattacharya, H. Hahn, B. Breitung, *Nat. Commun*. **2018**, *9*, 3400.
2. N. Qiu, H. Chen, Z. Yang, S. Sun, Y. Wang, Y. Cui, *J. Alloys Compd*. **2019**, *777*, 767.
3. H. Chen, N. Qiu, B. Wu, Z. Yang, S. Sun, Y. Wang, *RSC Adv*. **2019**, *9*, 28908.
4. E. Lokcu, C. Toparli, M. Anik, *ACS Appl. Mater. Interface* **2020**, *12*, 23860.
5. P. Ghigna, L. Airoldi, M. Fracchia, D. Callegari, U. A.Tamburini, P. D'Angelo, N. Pianta, R. Ruffo, G. Cibin, D.O. de Souza, E. Quartarone, *ACS Appl. Mater. Interfaces* **2020**, *12*, 50344.
6. T. Y. Chen, S. Y. Wang, C. H. Kuo, S. C. Huang, M. H. Lin, C. H. Li, H. Y. T. Chen, C. C. Wang, Y. F. Liao, C. C. Lin, Y. M. Chang, J. W. Yeh, S. J. Lin, T. Y. Chen, H. Y. Chen, *J. Mater. Chem. A* **2020**, *8*, 21756.
7. T. X. Nguyen, J. Patra, J. K. Chang, J. M. Ting, *J. Mater. Chem. A* **2020**, *8*, 18963.
8. D. Wang, S. Jiang, C. Duan, J. Mao, Y. Dong, K. Dong, Z. Wang, S. Luo, Y. Liu, X. Qi, *J. Alloys Compd.* **2020**, *844*, 156158.
9. C. Duan, K. Tian, X. Li, D. Wang, H. Sun, R. Zheng, Z. Wang, Y. Liu, *Ceram. Int*. **2021**, *47*, 32025.
10. H. Z. Xiang, H. X. Xie, Y. X. Chen, H. Zhang, A. Mao, C. H. Zheng, *J Mater Sci* **2021**, *56*, 8127.
11. M. Kheradmandfard, H. Minouei, N. Tsvetkov, A. K. Vayghan, S. F. K. Bozorg, G. Kim, S. I. Hong, D. E. Kim, *Mat. Chem. Phys*. **2021**, *262*, 124265.
12. J. Wei, K. Rong, X. Li, Y. Wang, Z. A. Qiao, Y. Fang, S. Dong, *Nano Res*. **2021**, *15*, 2756.
13. C. Y. Huang, C. W. Huang, M. C. Wu, J. Patra, T. X. Nguyen, M. T. Chang, O. Clemens, J. M. Ting, J. Li, J. K. Chang, *Chem. Eng. J*. **2021**, *420*, 129838.
14. J. Zhao, X. Yang, Y. Huang, F. Du, Y. Zeng, *ACS Appl. Mater. Interfaces* **2021**, *13*, 58674.
15. B. Xiao, G. Wu, T. Wang, Z. Wei, Y. Sui, B. Shen, J. Qi, F. Wei, Q. Meng, Y. Ren, X. Xue, J. Zheng, J. Mao, K. Dai, *Ceram. Int*. **2021**, *47*, 33972.

16. H. Chen, N. Qiu, B. Wu, Z. Yang, S. Sun, Y. Wang, *RSC Adv*. **2020**, *10*, 9736.
17. T. X. Nguyen, C. C. Tsai, J. Patra, O. Clemens, J. K. Chang, J. M. Ting, *Chem. Eng. J*. **2020**, *430*, 132658.
18. J. Patra, T. X. Nguyen, C. C. Tsai, O. Clemens, J. Li, P. Pal, W. K. Chan, C. H. Lee, H. Y. T. Chen, J. M. Ting, J. K. Chang, *Adv. Funct. Mater*. **2022**, *32*, 2110992.
19. H. Minouei, N. Tsvetkov, M. Kheradmandfard, J. Han, D. E. Kim, S. I. Hong, *J. Power Sources* **2022**, *549*, 232041.
20. J. Z. Yen, Y. C. Yang, H. Y. Tuan, *Chem. Eng. J.* **2022**, *450*, 137924.
21. Y. Zheng, X. Wu, X. Lan, R. Hu, *Processes* **2022**,*10*,49.
22. B. Xiao, G. Wu, T. Wang, Z. Wei, Y. Sui, B. Shen, J. Qi, F. Wei, J. Zheng, *Nano Energy* **2022***, 95*, 106962.
23. H. Guo, J. Shen, T. Wang, C. Cheng, H. Yao, X. Han, Q. Zheng, *Ceram. Int*. **2022**, *48*, 3344.
24. S. Li, Z. Peng, X. Fu, *J. Adv. Ceram*. **2023**. https://doi.org/10.26599/JAC.2023.9220666

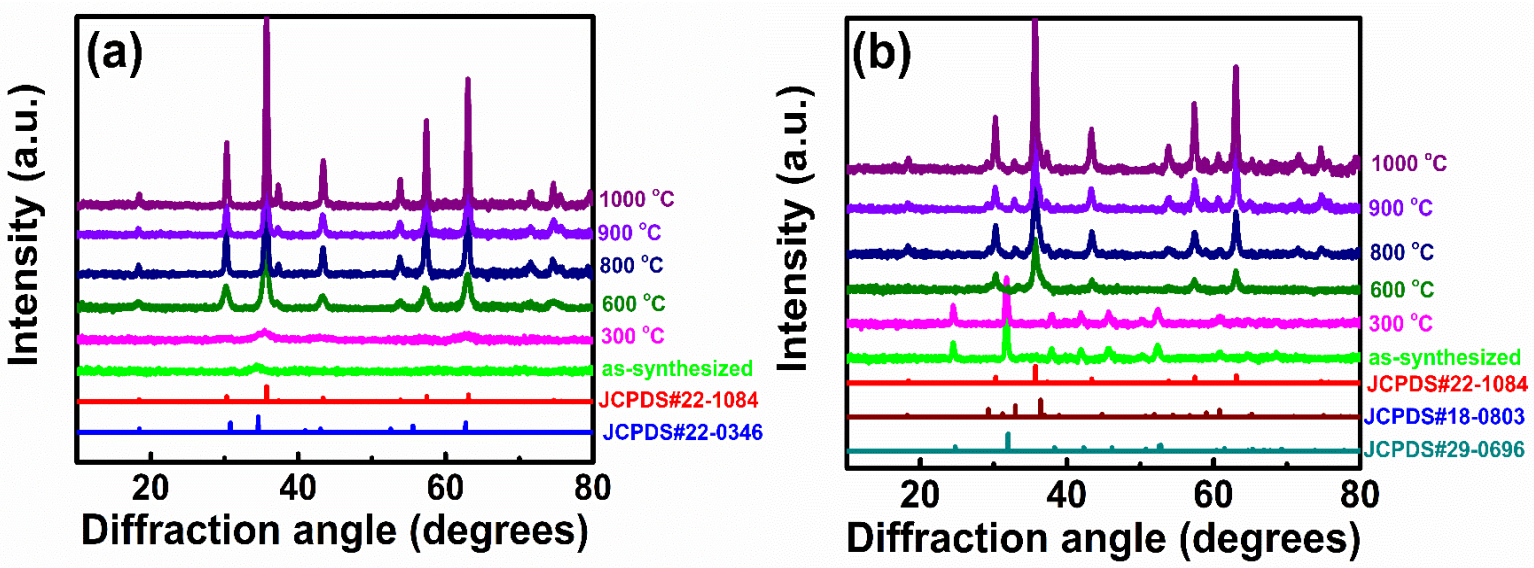

Figure S1. Structural evolution of (a) HESO (C) and (b) HESO (C+T) with increasing annealing temperature examined using XRD.

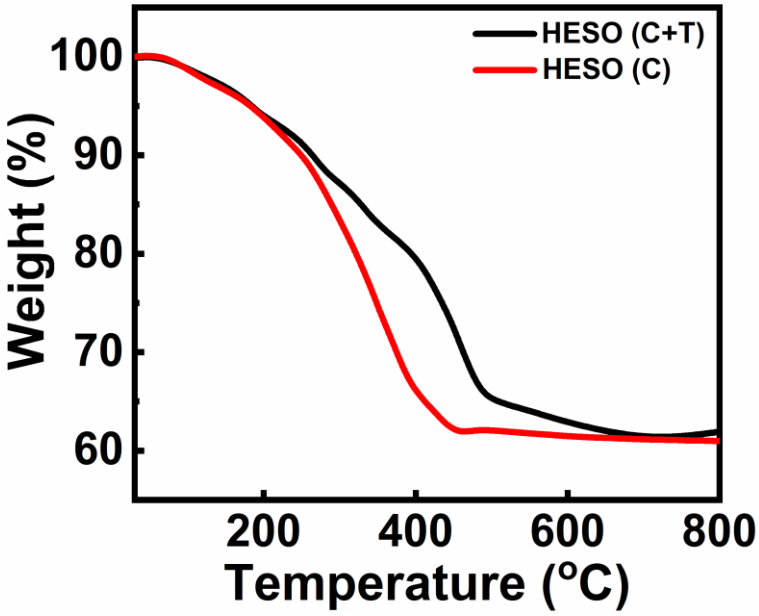

Figure S2. Thermogravimetric analysis data of HESO (C) and HESO (C+T).

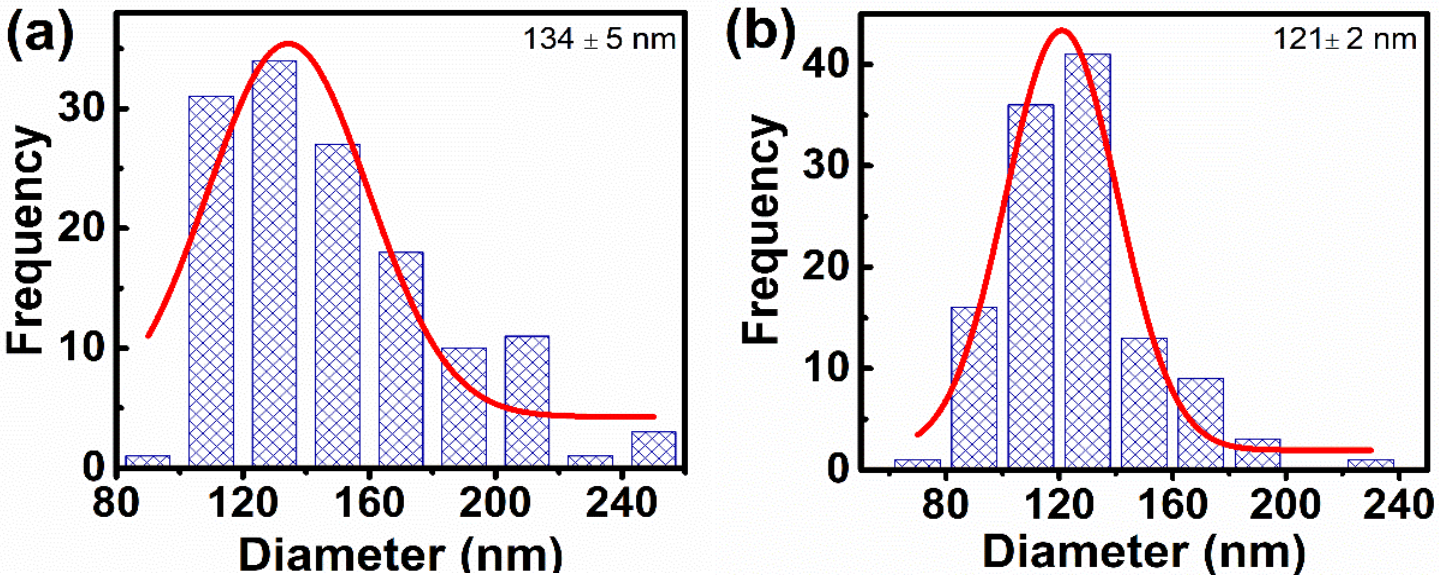

Figure S3. Particle size distribution of (a) HESO (C) and (b) HESO (C+T) examined using SEM.

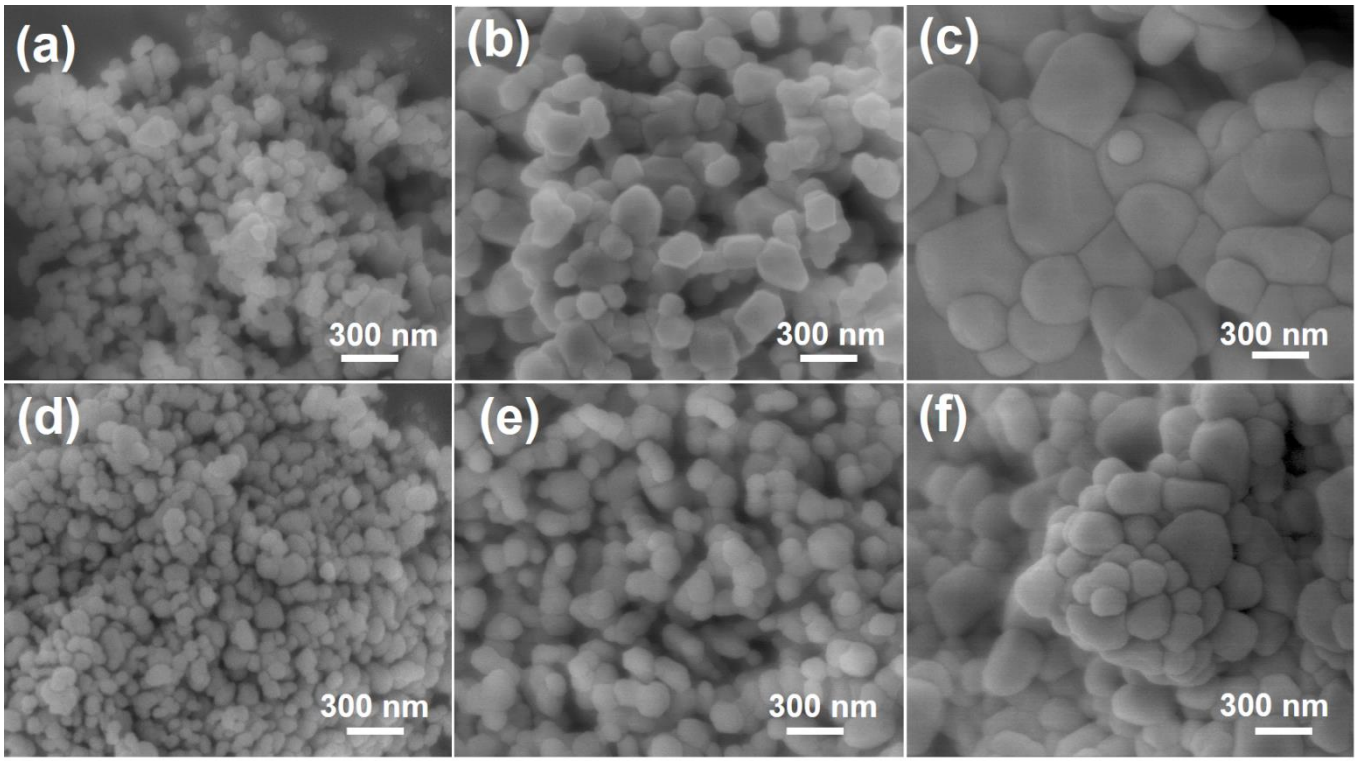

Figure S4. SEM images of HESO (C) annealed at (a) 800 °C, (b) 900 °C, and (c) 1000 °C. SEM images of HESO (C+T) annealed at (d) 800 °C, (e) 900 °C, and (f) 1000 °C.

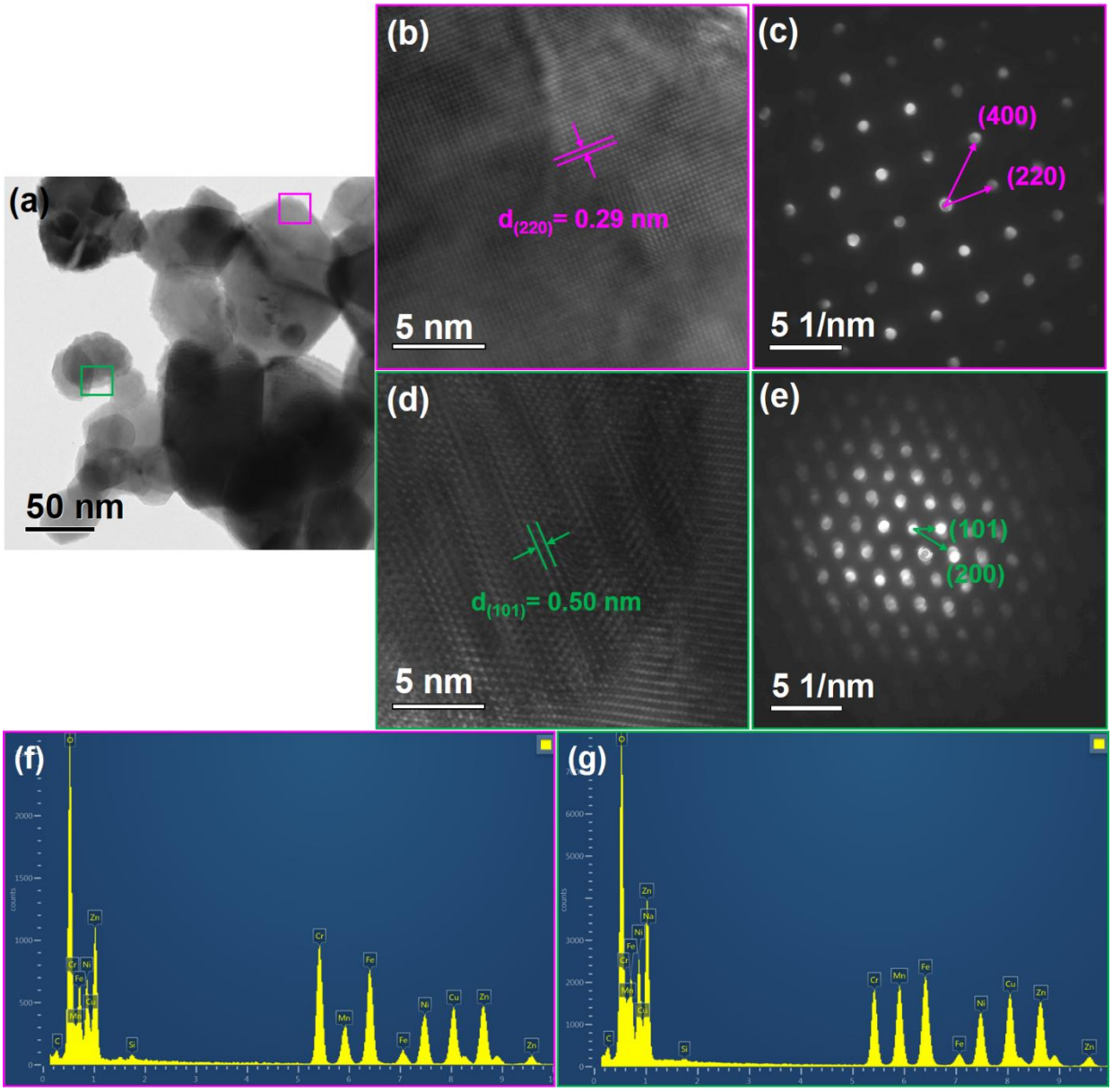

Figure S5. (a) Low-magnification TEM image of HESO (C+T), (b) HRTEM image and (c) SAED patern of cubic spinel phase, and (e) HRTEM image and (c) SAED patern of tetragonal spinel phase. EDS spectra of (f) cubic spinel and (g) teragonal spinel phases.

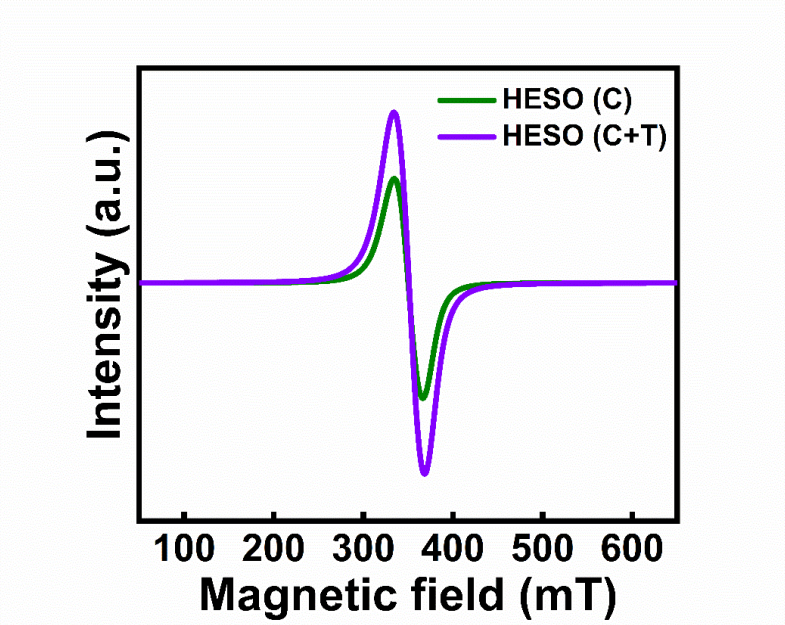

Figure S6. Electron paramagnetic resonance data of HESO (C) and HESO (C+T) samples.

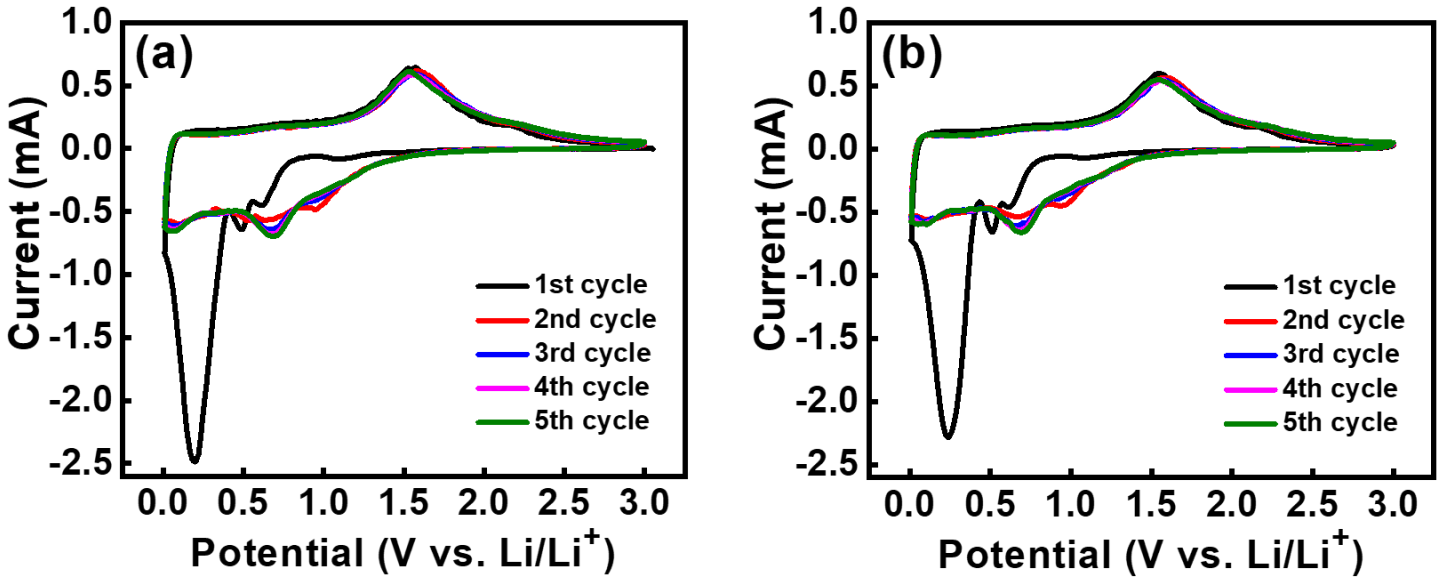

Figure S7. CV curves of (a) HESO (C) and (b) HESO (C+T) electrodes recorded at a potential sweep rate of 0.1 mV s^{-1}.

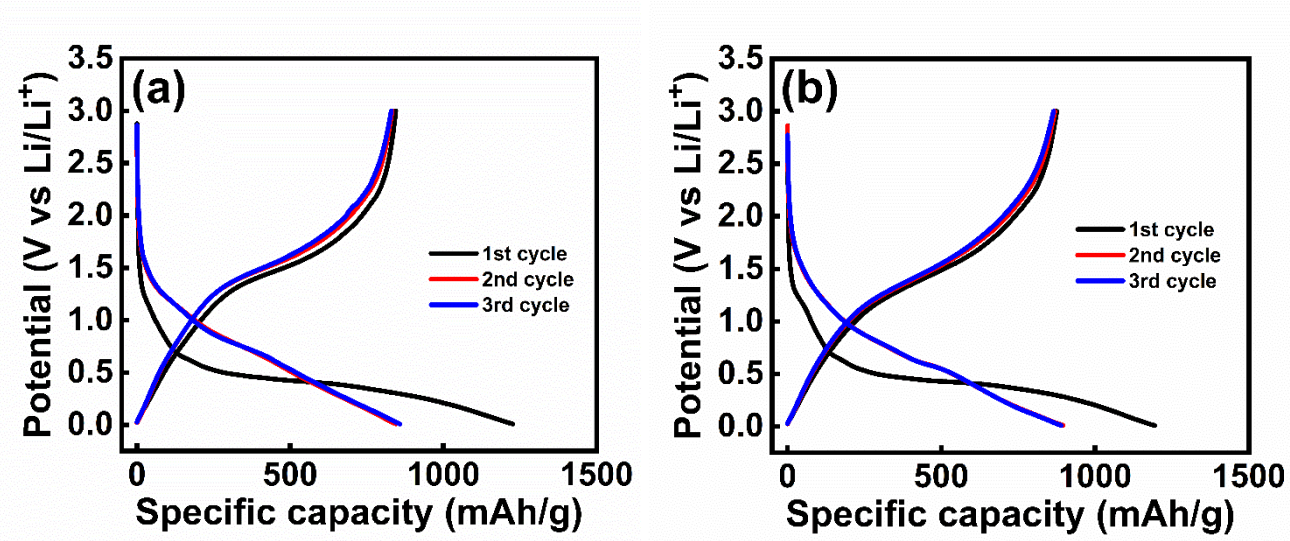

Figure S8. Initial charge-discharge cycles of (a) HESO (C) and (b) HESO (C+T) measured at 50 m Ag^{-1}.

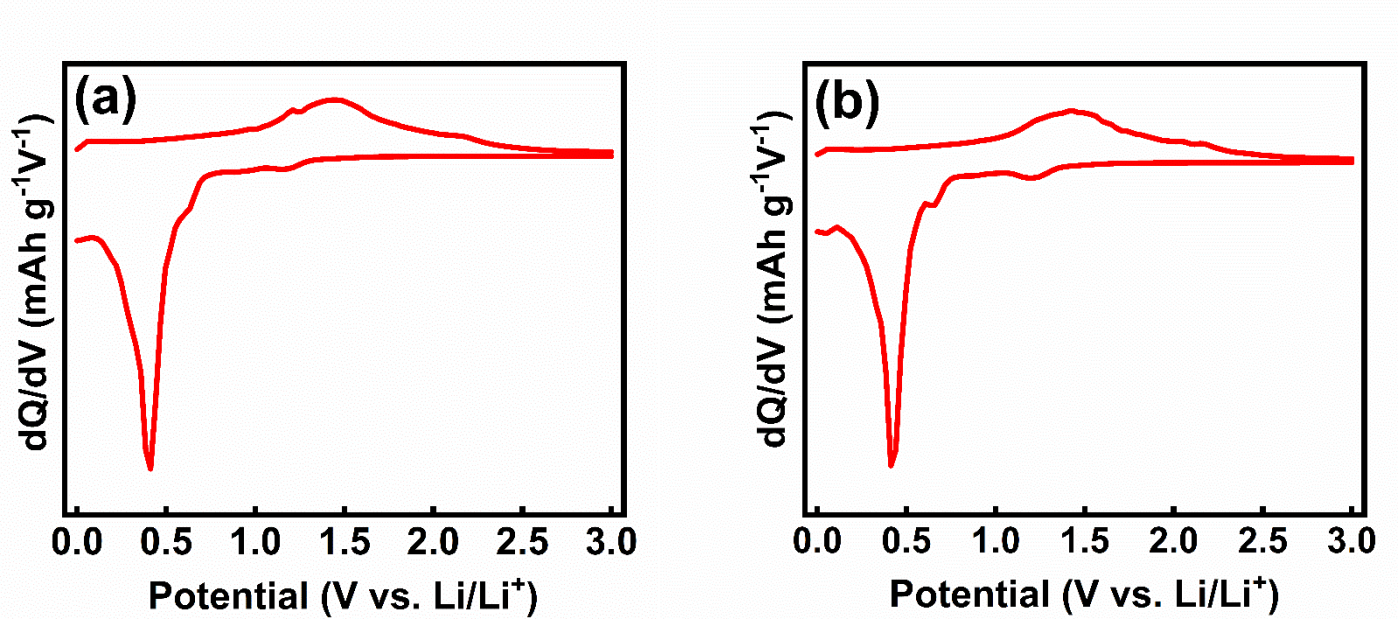

Figure S9. Differential capacity vs. voltage (dQ/dV) curves for (a) HESO (C) and (b) HESO (C+T) electrodes.

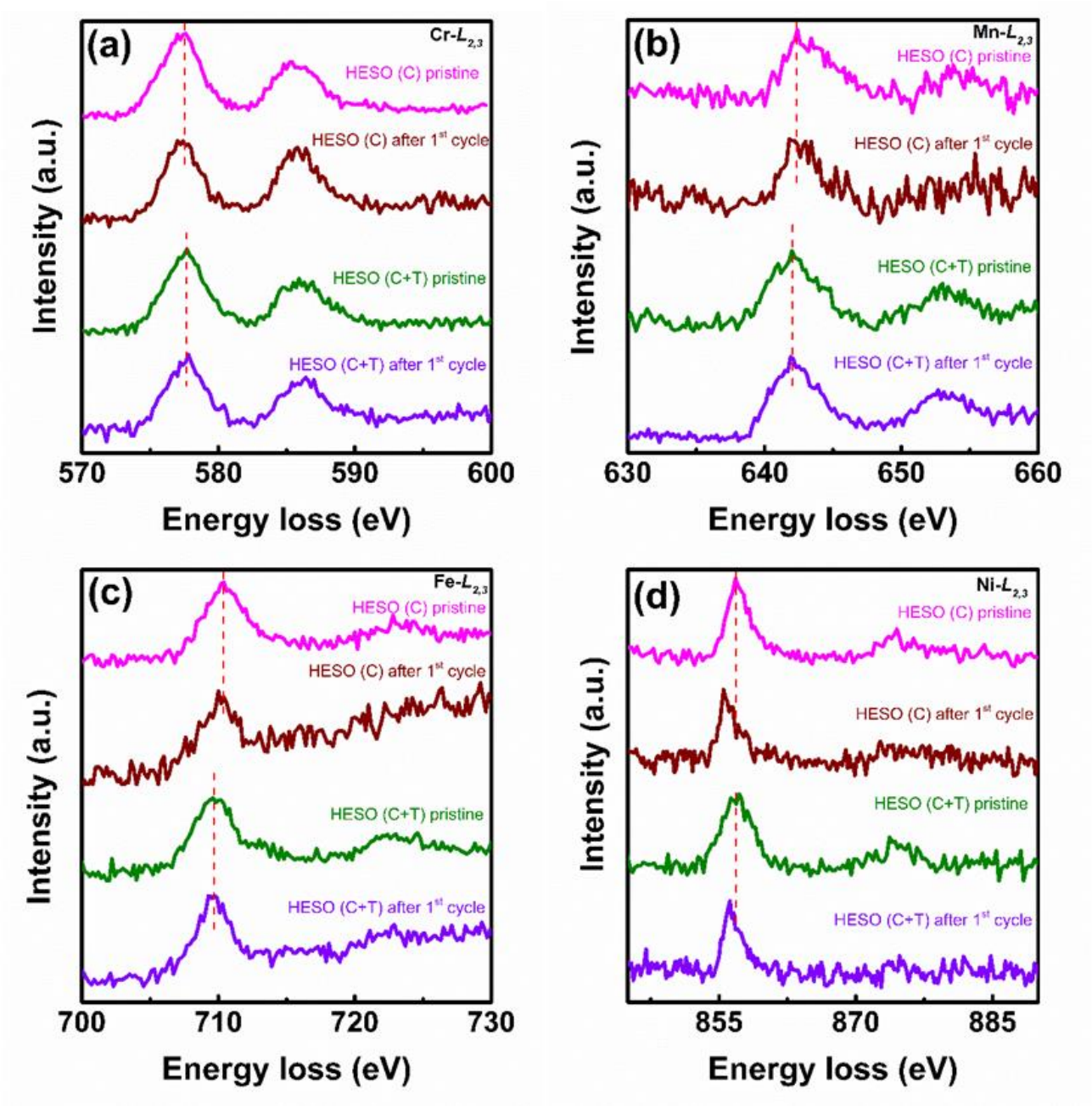

Figure S10. EELS data of HESO electrodes before and after the first charge-discharge cycle. EELS L-edge spectra of (a) Cr, (b) Mn, (c) Fe, and (d) Ni elements.

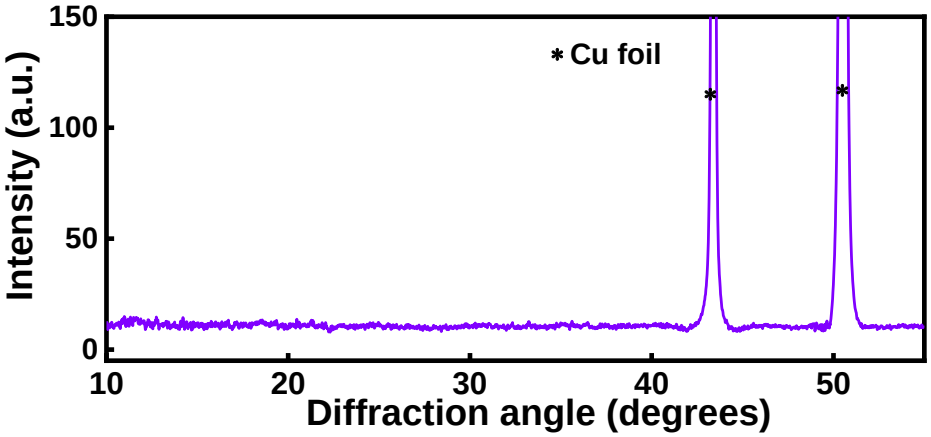

Figure S11. Ex-situ XRD measurement carried out after complete lithiation of the HESO (C+T) electrode.

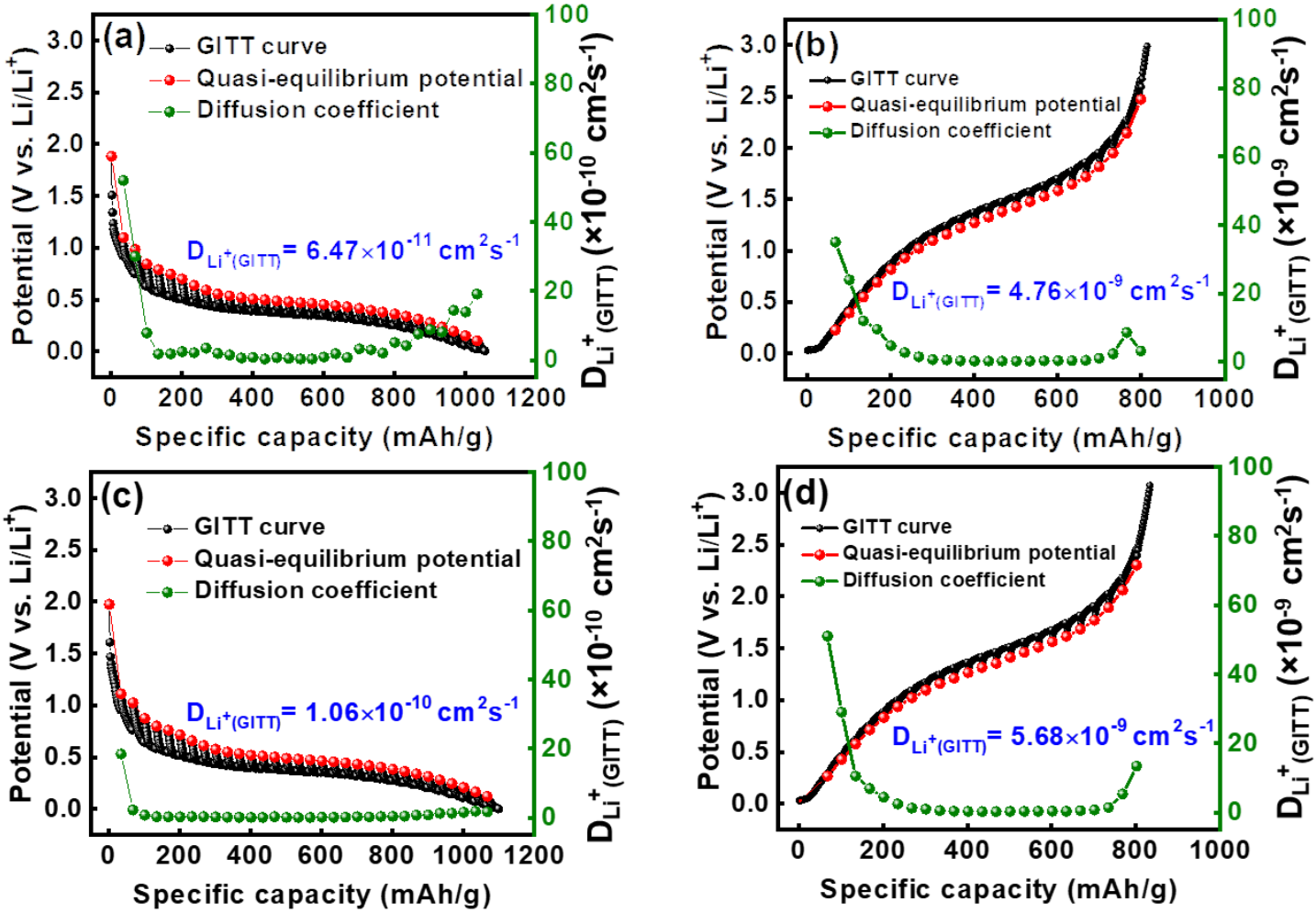

Figure S12. GITT results of HESO (C) ((a) and (b)) and HESO (C+T) electrodes ((c) and (d)). (a) and (c) represent lithiation properties; (b) and (d) represent delithiation properties. Data were recorded with a series of current pulses of 100 mA g^{-1} for 20 min and 3 h relaxation at each interval.

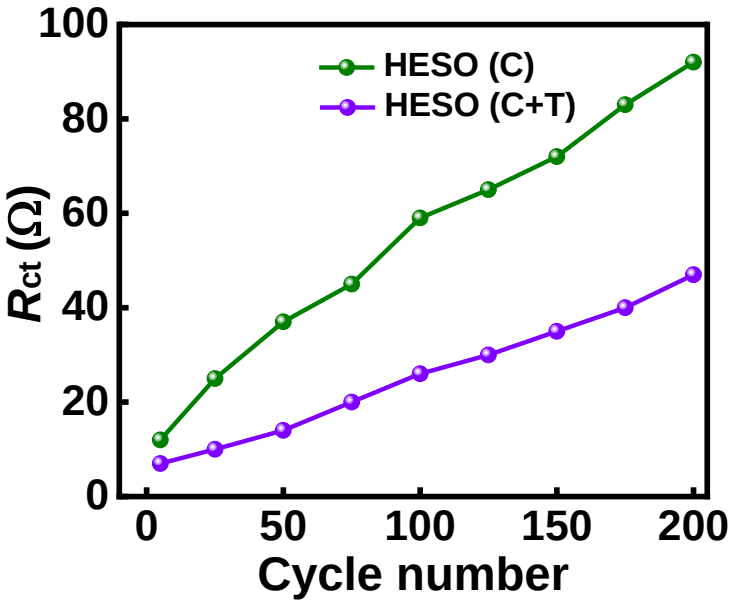

Figure S13. Variations of R_{ct} versus cycle number for HESO (C) and HESO (C+T) electrodes.